J. Fluid Mech. (2014), *vol.* 747, *pp.* 656–687. © Cambridge University Press 2014
doi:10.1017/jfm.2014.156

Experimental investigation of aerofoil tonal noise generation

S. Pröbsting[1],†, **J. Serpieri**[1,2] **and F. Scarano**[1]

[1]Department of Aerospace Engineering, Delft University of Technology, Delft, 2629 HS, The Netherlands

[2]Department of Industrial Engineering, University of Naples Federico II, Naples, 80125, Italy

(Received 5 September 2013; revised 6 March 2014; accepted 17 March 2014;
first published online 23 April 2014)

The present study investigates the mechanisms associated with tonal noise emission from a NACA 0012 aerofoil at moderate incidence (0°, 1°, 2° and 4° angle of attack) and with Reynolds numbers ranging from 100 000 to 270 000. Simultaneous time-resolved particle image velocimetry (PIV) of the aeroacoustic source region near the trailing edge and acoustic measurements in the far field are performed in order to establish the correspondence between the flow structure and acoustic emissions. Results of these experiments are presented and analysed in view of past research for a number of selected cases. Characteristics of the acoustic emission and principal features of the average flow field agree with data presented in previous studies on the topic. Time-resolved analysis shows that downstream convecting vortical structures, resulting from growing shear layer instabilities, coherently pass the trailing edge at a frequency equal to that of the dominant tone. Therefore, the scattering of the vortical structures and their associated wall pressure fluctuations are identified as tone generating mechanisms for the cases investigated here. Moreover, wavelet analysis of the acoustic pressure and velocity signals near the trailing edge show a similar periodic amplitude modulation which is associated with multiple tonal peaks in the acoustic spectrum. Periodic amplitude modulation of the acoustic pressure and velocity fluctuations on the pressure side are also observed when transition is forced on the suction side, showing that pressure-side events alone can be the cause.

Key words: aeroacoustics, boundary layer stability, vortex shedding

1. Introduction and background

Tonal noise produced by aerofoils at moderate Reynolds numbers is a very marked aeroacoustic phenomenon and, as such, it has triggered research interest for several decades. The earliest reports date back to the work of Hersh & Hayden (1971), and the work is clearly not closed considering the very recent studies of Tam & Ju (2012) and Plogmann, Herrig & Würz (2013). Aerofoils operating in such conditions can be found in micro-wind turbines as well as in compressors, cooling fans and other rotating machinery (Wright 1976; Arcondoulis *et al.* 2010). While self-noise generated by aerofoils at high Reynolds numbers in an undisturbed flow and in the absence of

---

† Email address for correspondence: s.probsting@tudelft.nl

separation is dominated by the interaction of the turbulent boundary layers with the trailing edge (Roger & Moreau 2010), tones produced at moderate Reynolds numbers are often associated with the growth and convection of unstable waves in the laminar boundary layer (Arbey & Bataille 1983).

1.1. *Early observations and scaling rules*

The acoustic spectrum shows a number of particular features. For a range of aerofoils at moderate Reynolds numbers the spectrum exhibits a 'ladder'-type structure in its dependence on the free stream velocity: a broadband hump is centred at a certain frequency f_s and superimposed by a set of discrete tones at frequency f_n, where n indicates the ordinal number of the tone. Observations showed the tonal frequency of highest intensity $f_{n_{max}}$ to be close to the broadband centre frequency f_s, which follows a different scaling behaviour with free stream velocity ($\sim u^{1.5}$) when compared to individual tones f_n ($\sim u^{0.8}$). Moreover, a transition of the maximum intensity between these discrete tones f_n has been observed with increasing velocity (Arbey & Bataille 1983). Thus the dominant tone $f_{n_{max}}$ follows a dependency of $u^{0.8}$ over finite ranges of Reynolds numbers (constant n) with jumps in between (change of n), resulting in an overall trend following a dependency on $u^{1.5}$. This particular behaviour has been denoted as a 'ladder' structure with transitions of n creating the 'rungs'.

Since the structure of the tonal noise emitted by aerofoils at moderate Reynolds numbers was observed by Hersh & Hayden (1971) and later Paterson *et al.* (1973), a number of justifications and physical models have been proposed. However, no absolute agreement on the physical mechanism for the discrete tonal noise, and more specifically for the 'ladder' type structure of the spectrum, has been achieved. Instead, much controversy has been generated in the discussion.

Early works focused on the characterization of acoustic emissions under such conditions, and scaling rules for the tonal and broadband noise components were proposed. Paterson *et al.* (1973) conducted measurements on an aerofoil profile and identified individual tones up to a Reynolds number of approximately $Re = 10^6$, finding evidence for the 'ladder'-type behaviour of the spectrum as a function of Reynolds number. The occurrence of tones was ascribed to the presence of a laminar boundary layer on the pressure side of the aerofoil near the trailing edge and an empirical scaling rule for the average frequency variation was proposed, justified on the basis of a vortex shedding:

$$f_s \approx 0.011 u^{3/2}/(c\nu)^{1/2}. \tag{1.1}$$

Here, u denotes the free stream velocity, c the chord and ν the kinematic viscosity. Tam (1974) stated that vortex shedding alone was inadequate, as it does not explain the selection of discrete tones, and instead proposed the concept of a feedback loop between a noise source in the wake and the flow at the trailing edge. The noise source comprises shed vorticity from both sides of the aerofoil and an interaction in the near wake.

A feedback model leads to the introduction of a free integer parameter n, which is required for the description of the phase condition. Based on the experimental data of Paterson *et al.* (1973) a scaling law for the discrete tones of the following form was proposed, where k is a constant of proportionality depending on geometry and angle of attack:

$$f_n = knu^{0.8}. \tag{1.2}$$

It should be noted, however, that the exponent claimed by Paterson *et al.* (1973) and Tam (1974), namely $n = 0.8$, is not universally adapted. For instance, Arbey & Bataille (1983) report a value of 0.85. The latter authors also explained the shape of the overall spectrum by a decomposition into tonal components f_n (1.2) and the broadband component, centred on f_s (1.1), whose summation results in a single dominant tone $f_{n_{max}}$.

The study of Atobe, Tuinstra & Takagi (2009), conducted in a resonant environment, showed a fundamentally different velocity dependence. In contrast to the experiments conducted in anechoic facilities, tonal frequencies were reported to remain constant with increasing velocity, which was attributed to resonance effects. This study underlines the sensitivity of experimental results towards the laboratory environment and experimental conditions. In a recent review on the topic, Arcondoulis *et al.* (2010) mentioned that, for instance, the free stream turbulence can be an important factor, promoting or delaying transition in the low-Reynolds-number regime.

1.2. *The role of boundary layer instabilities*

Arbey & Bataille (1983) investigated the case of a NACA 0012 aerofoil with models of different chord length at zero incidence. The narrowband contribution of the acoustic spectrum, centred around a peak at frequency f_s, was similar to that of the wall pressure spectrum and ascribed to the diffraction of instabilities, developing in the boundary layer, at the trailing edge through the mechanism described by Howe (1978). The centre frequency of the broadband noise was associated with a Strouhal number, based on the boundary layer thickness at the trailing edge, of $St = 0.048$, constant with Reynolds numbers. They introduced a phase condition involving discrete frequencies similar to that of Tam (1974), but based on the concept of Fink (1975), where L is the distance between the point of maximum velocity on the aerofoil and the trailing edge as the noise source, c_r the propagation speed of Tollmien–Schlichting (T–S) waves, and c_0 the speed of sound.

$$f_n L/c_r(1 + c_r/(c_0 - u)) = n + 1/2. \tag{1.3}$$

Determining the length scale L has since then been a subject of controversy and Chong & Joseph (2012) have noted that the point of first instability might be chosen more appropriately.

Following Arbey & Bataille (1983), attention was paid to the role of instabilities in the noise generation process. Aizin (1992) performed an analytical study, investigating the generation of noise by T–S waves. They found that the acoustic pressure at the frequency of the T–S waves is proportional to the wall pressure fluctuations near the trailing edge, confirming the assertions of Arbey & Bataille (1983) regarding the role of T–S waves in trailing edge noise generation. The hypothesis is further supported by Sandberg *et al.* (2009), who performed direct numerical simulations (DNS) on a series of NACA aerofoils at various angles of attack and applied diffraction theory (Amiet 1976) to estimate the sound pressure level. A good agreement with the reference solution led them to the conclusion that pressure fluctuations convecting past the trailing edge are the primary noise source. A further study taking into account different conditions gave additional confirmation for the latter hypothesis (Jones & Sandberg 2011).

Hersh & Hayden (1971), and later Paterson *et al.* (1973), performed experiments applying a tripping device to force transition on both the pressure and suction sides separately. While changes on the suction side were found to have only a small effect on the tonal noise generation, the turbulent boundary layer on the pressure side of the aerofoil led to the suppression of tonal noise. They concluded that the instabilities in the laminar boundary layer on the pressure side are essential to tonal noise generation. Subsequently, Fink (1975) performed experiments on a flat plate and found evidence of laminar boundary layer instabilities on pressure side. They suggested a feedback loop between the noise generated at the trailing edge and the instabilities in the boundary layer. Recent work of Plogmann *et al.* (2013) provides strong experimental evidence for the existence of such a feedback loop.

In laser Doppler velocimetry measurements on various aerofoils, McAlpine, Nash & Lowson (1999) observed a separation bubble on the pressure side near the trailing edge and proposed its presence as a necessary condition for discrete tones to occur. Furthermore, their measurements implied that the intensity of the discrete tones is related to the extent of the separation bubble. In a related study, Nash, Lowson & McAlpine (1999) pointed out that a region of separated flow might exist without discrete tones being present. Therefore, the conditions of Lowson, Fiddes & Nash (1994), requiring the presence of flow separation, may be regarded as necessary but not sufficient for discrete tones to occur.

1.3. *Amplitude modulation*

Numerical simulations have been applied, for instance, by Desquesnes, Terracol & Sagaut (2007), Sandberg *et al.* (2009), Sandberg & Jones (2011), Ikeda, Atobe & Takagi (2012) and Tam & Ju (2012). Almost all studies were performed assuming two-dimensional flow, therefore omitting the possibility of three-dimensional instabilities.

The work of Desquesnes *et al.* (2007) is of particular relevance, as the current study arises from the conclusions of their numerical investigation. Their results support the earlier hypothesis that the dominant tone frequency is associated with boundary layer instabilities passing the trailing edge. At the trailing edge, acoustic waves are scattered, sustaining a feedback mechanism with the susceptible part of the laminar boundary layer. A transient analysis based on the short-time Fourier transform of the acoustic signal showed that the tones in the acoustic power spectrum are due to an almost periodic amplitude modulation of the dominant tone.

This modulation has been associated with the varying phase difference between aerodynamic fluctuations on the two sides of the aerofoil near the trailing edge. It is conjectured that an interaction of the most amplified frequencies at the pressure and suction sides is necessary for the occurrence of multiple tones. To date, no experimental evidence for the transient behaviour of aerodynamic velocity fluctuations has been obtained, thus motivating the present study.

1.4. *Present study*

The amplitude modulation resulting in multiple tones can be explained by mechanisms other than the phase variation discussed by Desquesnes *et al.* (2007). It is expected that an inspection of the flow field organization and temporal evolution near the trailing edge can provide answers to the following questions:

(*a*) Can the amplitude modulation of the acoustic pressure, observed in a numerical simulation by Desquesnes *et al.* (2007), be confirmed experimentally?

(*b*) Is this amplitude modulation also present in the velocity field near the trailing edge?

(*c*) What is the importance of the phase delay between the two sides of the aerofoil for the generation of tonal noise?

(*d*) Are multiple discrete tones present under the condition of forced transition on one side of the aerofoil or dependent on a two-sided feedback loop (Desquesnes *et al.* 2007)?

To address the above questions, it is necessary to study the generated noise as well as the structure and dynamical evolution of the flow field near the trailing edge. For this purpose we chose to use time-resolved particle image velocimetry (PIV).

The use of PIV as a complementary diagnostic tool in aeroacoustics has been already proved in a number of studies, as discussed in a review by Morris (2011). Schröder *et al.* (2006) performed a study on trailing edge noise sources using time-resolved PIV. Phase-locked PIV provides an alternative for the assessment of the flow field within the source region and has been applied, for instance, by Shannon & Morris (2006) for the study of noise generated at the blunt trailing edge of a flat plate. Using the same technique, Nakano, Fujisawa & Lee (2006) focused on the subject of boundary layer instability noise and showed the zero time-shift correlation of velocity fluctuations and acoustic pressure acquired by simultaneous PIV and microphone measurements. They were also able to identify the relationship between the dominant frequency of the acoustic pressure and fluctuations on the pressure side of the aerofoil and in the near-wake. Although phase-locked analysis is a powerful statistical tool, the underlying hypothesis is that the system oscillates with a single phase, but intermittent or transient phenomena as well as spectral properties cannot be accessed. With time-resolved PIV analysis the study of the spatio-temporal evolution is possible, which, for instance, also allows the observation of transient behaviour and temporally coherent structures.

2. Experimental set-up

A NACA 0012 aerofoil of $c = 100$ mm chord length and 400 mm span is installed in the low-speed V-Tunnel at Delft University of Technology, an open-section low-turbulence wind tunnel with a circular cross-section of diameter 600 mm, operating in the velocity range between 5 and 45 m s^{-1} with free stream turbulence intensity below 1 %.

The aerofoil is manufactured from acrylic glass with a polished surface, allowing light transmission and the simultaneous illumination of both sides. It is installed vertically at the centre of the wind tunnel, 150 mm above the nozzle exit, and the angle of attack is adjusted through rotation about the quarter chord point.

The free stream velocity is varied between 16 and 40 m s^{-1} and the aerofoil is placed at incidence $\alpha = 0^\circ, 1^\circ, 2^\circ$ and 4°. The resulting Reynolds numbers are 10^5 and 2.7×10^5 for the lowest and highest velocity, respectively. As a tripping device, 3D roughness elements (carborundum, 0.8 mm height) have been applied on the suction side at $0.2c$.

Since the aerofoil is placed in a free jet, the effective angle of attack is lower than the geometric angle due to flow curvature and downward deflection of the stream. This effect has only been partially considered in the past – for instance, no correction is indicated by Paterson *et al.* (1973) and Nash *et al.* (1999). The reason for this omission might be a relatively small blockage ratio, which is also the case for the present study. Following the procedure of Brooks, Pope & Marcolini (1989), by assuming a rectangular test section of 0.4 m × 0.4 m, equal to the distance between the restraining side plates and a conservative estimate for the dimensions of the

	Case 1	Case 2	Case 3
u_∞ (m s^{-1})	24	24	24
α	2°	2°	4°
$\alpha^\star$	1.5°	1.5°	2.9°
x_{tr}/c	—	0.2	—

TABLE 1. Parameters of the experiments with associated PIV data analysis. Here x_{tr}/c denotes the relative position projected on the chord line of the tripping device on the suction side of the aerofoil for case 3.

square enclosed by the round test section, the correction factor for the effective angle of attack based on a blockage ratio of $0.012/0.4 = 0.03$ is $\alpha^\star/\alpha = 0.72$.

From the PIV data analysis three cases are presented here: case 1 denotes the configuration with free stream velocity 24 m s^{-1} and geometrical angle of attack $\alpha = 2°$. Case 2 comprises identical conditions, but forced transition on the suction side. For case 3 a free stream velocity of 24 m s^{-1} and an angle of attack 4° apply (table 1).

2.1. *Acoustic measurements*

Two LinearX M51 microphones are positioned on opposite sides of the aerofoil at a distance of 1.1 m and perpendicular to the chord plane at the level of the trailing edge. Nominally, the microphones feature a flat frequency response between 50 Hz and 20 kHz. The microphones are calibrated with a GRAS piston phone.

Measurements are performed at a sampling frequency of 40 kHz for a period of 20 s for statistical purposes. To process the statistical data, the coherent output power (COP) method (Hutcheson & Brooks 2002), previously applied for the measurement of trailing edge noise by Brooks & Hodgson (1981), filters the incoherent part of the signal under the assumption of uniform directivity. If not mentioned otherwise, power spectra are computed using an average periodogram method (Welch 1967), where a Hamming windowing function is applied to each segment of the original signal (Harris 1978). For the COP the cross-power spectra for the signals of the symmetrically arranged microphones are considered instead of auto power spectra. The number of samples per window is 16 384 and an overlap of 50 % is applied, resulting in a frequency resolution of 2.44 Hz. For transient analysis and correlation, data is acquired simultaneously with the PIV measurements. The wavelet transform of a single microphone signal is computed following Torrence & Compo (1998).

2.2. *PIV measurements*

The airflow is seeded with water–glycol-based fog particles of mean diameter 1 μm. Illumination is provided by a Litron Nd:YLF laser (80 W, dual cavity). The measurement domain (approximately 3.2×1.6 cm^2) includes the flow upstream and downstream of the trailing edge on both sides of the aerofoil (figure 1). Illumination through the trailing edge is affected by local refraction, causing a shadowed region on the opposite side where data is not available.

A Photron FastCam SA1.1 (1024 × 1024 pixels (px), 12 bits, pixel pitch 20 μm) equipped with a Nikon Micro-Nikkor 200 mm prime lens was used and operated at a focal ratio $f/4$. The optical magnification is $M = 0.65$, leading to a digital imaging

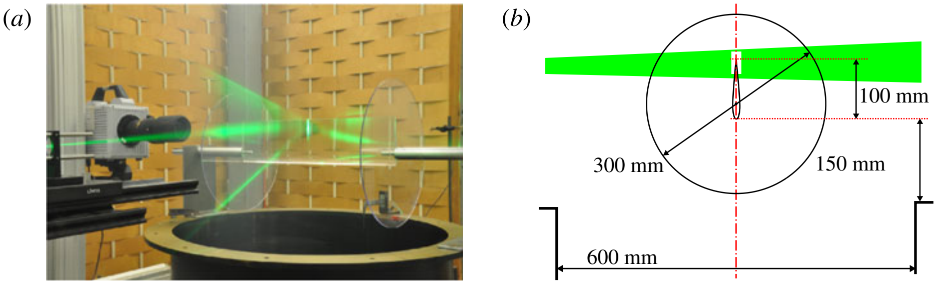

FIGURE 1. (Colour online) Experimental arrangement (*a*) and schematic of the PIV experiment (*b*).

resolution of 32 px mm^{-1}. With this aperture the diffraction-limited particle image diameter is estimated to be less than 1 pixel at the plane of focus (diffraction spot size $d_{diff} = 9\ \mu\text{m}$), which would lead to unresolved particle images and a consequent large bias error due to peak-locking. Therefore, the plane of focus is slightly shifted away from the illumination plane, leading to defocused particle images encompassing approximately 2–3 px, which eliminates peak-locking errors.

The measurement system is controlled by a PC workstation, equipped with a LaVision HighSpeed Controller that synchronizes illumination and imaging devices, and operated by the LaVision DAVIS 8 software, which is also used for image pre-processing and interrogation. In double-frame mode, the acquisition frequency for image pairs is $f_{acq} = 6$ kHz. The pulse separation is adjusted such that the particle displacement in the free stream is approximately equal to 0.47 mm (15 px in the image plane). Sequences are recorded for a duration of 1.16 s, equivalent to 6970 image pairs contained in each sequence. Table 2 summarizes the parameters of the PIV measurements.

Assuming a random error of 0.1 px on the localization of the correlation peak, which is typically reported for planar PIV experiments (Raffel *et al.* 2007), the relative random error on the velocity can be estimated as $\sigma/u_\infty = 0.1/15 = 0.007$ in the free stream.

Images are processed using an iterative multi-grid multi-pass technique with window deformation and a final window size of 0.5 mm in physical space (16 px). The overlap factor is 75 %, resulting in a vector spacing of approximately 0.125 mm. To improve the spatial resolution in the wall-normal direction, Gaussian window weighting (aspect ratio 2:1) is applied during the correlation process (Scarano 2003).

For the x–y coordinate system, the origin is defined at the trailing edge and the direction of the abscissa coincides with that of the chord line for an aerofoil at zero angle of attack. Velocity components are denoted by u and v, respectively. The coordinates in the surface-attached coordinate system on the two sides of the aerofoil are denoted by x_t and x_n, where the abscissa is tangential to the surface of the aerofoil at the trailing edge. Here, velocity components are denoted by u_t and u_n, respectively.

3. Noise emission

As outlined in the introduction, the presence of tones depends upon a number of parameters, most importantly the Reynolds number and the angle of attack for the given aerofoil. The noise emission characteristics for the chosen aerofoil model are illustrated in this section, encompassing a significant range of flow conditions.

Parameter	Symbol	Value
Lens focal length		200 mm
Focal ratio	$f/\#$	4
Magnification	M	0.65
Field of view	FOV	32×16 mm^2
Acquisition frequency	f_{acq}	6 kHz
Free stream displacement	Δx	15 px
Measurement time	T	1.16 s
Number of samples	N	6970
Window size	Ws	0.5 mm
Vector spacing		0.125 mm
Vector grid		100×50

TABLE 2. Parameters for PIV experiments.

3.1. *Acoustic pressure power spectra*

Acoustic measurements are performed for angles of attack between 0° and 4°, and free stream velocities between 16 and 40 m s^{-1} ($Re = 1\text{–}2.7 \times 10^5$), sampled with a resolution of $u_\infty = 1$ m s^{-1}. The resulting dependence of the acoustic power spectra on the free stream velocity is depicted in figure 2. Acoustic power spectra based on the signal of a single microphone and the COP compare well (figure 3), with broadband levels of the latter case limited by the background noise of the facility at the respective free stream velocities.

The spectral map corresponding to the aerofoil at zero incidence shows a dominant tone in the range between 16 and 35 m s^{-1}. A harmonic between 25 to 40 m s^{-1} and likely at higher velocities corresponds to twice the previous frequency. Further harmonics with threefold and fourfold frequencies are present, but contain less energy. Tones, separated by a smaller difference in frequency are visible, especially for the experiments conducted at 30 m s^{-1} and above, and can be observed for the dominant tone and its upper harmonic.

Tones have been related to the concept of a feedback loop between convective instabilities and upstream propagating acoustic waves by a number of researchers (Tam 1974; Arbey & Bataille 1983). A feedback loop implies a phase condition (1.3) that allows only a discrete set of frequencies. The empirical fit to the relation $f_n \approx knu^{0.8}$ (1.2), indicated for $n = 5, \ldots, 12$ in figure 2, is often found to describe the development of individual tone frequencies. Comparison of the slopes reveals a dependence of the constant k in (1.2) on the angle of attack.

Based on the results of a DNS, Tam & Ju (2012) report only a single discrete tone for a NACA 0012 at zero angle of attack, inferring that the occurrence of multiple discrete tones in experimental studies must be related to the experimental facility and are not genuine for isolated aerofoils. For instance, the presence of free stream turbulence, but also small alignment inaccuracies ($\leqslant 0.1°$), might have an influence and their effect cannot be excluded in the present study. However, this conclusion applies only to the conditions of the above study, where the instability is evident only in the wake, in contrast to other studies (Desquesnes *et al.* 2007; Jones & Sandberg 2011; Plogmann *et al.* 2013) and the PIV observations in the present investigation.

The scenario is changed slightly at $\alpha = 1°$ angle of attack, but more clearly at $\alpha = 2°$, where multiple intermediate tones dominate the spectrum between 20 and 30 m s^{-1}

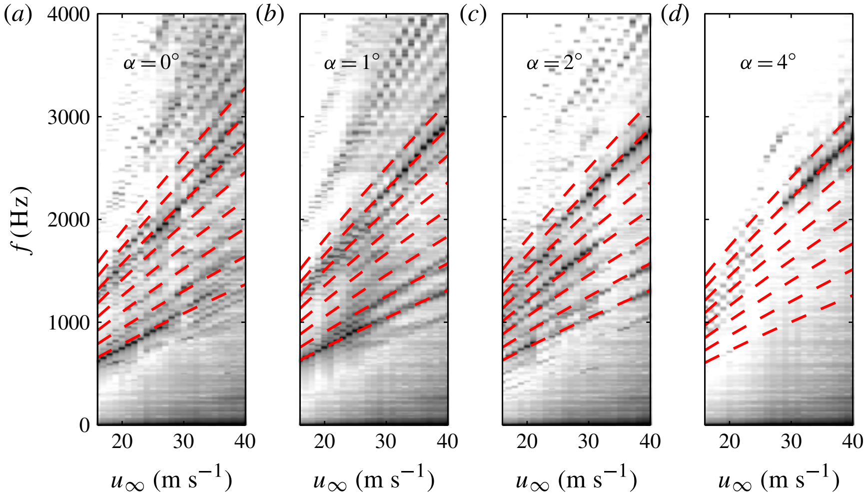

FIGURE 2. (Colour online) Dependence of the acoustic pressure power spectra on velocity and angle of attack. Dashed lines indicate fits based on the empirical relation (1.2) with $n = 5, \ldots, 12$ and $k = \{5.5, 5.3, 5.2, 5.1\}$ for $\alpha = \{0°, 1°, 2°, 4°\}$, respectively.

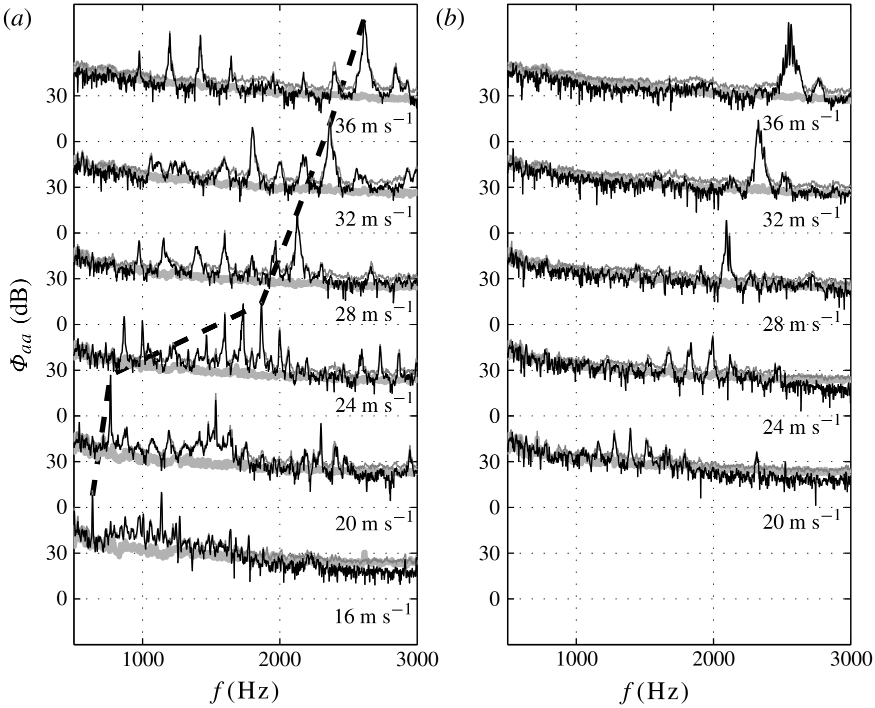

FIGURE 3. Power spectra of far-field acoustic pressure for the aerofoil at $\alpha = 2°$ (*a*) and $\alpha = 4°$ (*b*) for a single microphone (thin grey lines) and estimated using the coherent output power method for two microphones (black), with background noise levels indicated (thick grey lines). Additionally, for $\alpha = 2°$ the dominant tone frequency $f_{n_{max}}$ is indicated. Data acquired simultaneously with PIV measurements.

and transitions of the dominant tone frequency are evident. Also Desquesnes *et al.* (2007) observed tones at $Re = 2 \times 10^5$, based on the 2D DNS solution at the same angle of attack, and clearly identified the onset of the instability over the aerofoil and not only in the near-wake. These transitions of the dominant tone frequency provide evidence for the existence of a 'ladder' structure. At $\alpha = 2^\circ$, the main features of the velocity field presented by Desquesnes *et al.* (2007) agree with the PIV results of the present study, showing local flow separation and fast growth of unstable waves on the pressure side, and convecting vortical structures on the suction side near the trailing edge for this range of Reynolds numbers, as will be shown later. The extent of the separated flow region on the pressure side depends on Reynolds number and angle of attack. According to the feedback loop hypothesis these parameters influence the frequencies of the tones according to the phase condition given in (1.3).

At the largest angle of attack ($\alpha = 4^\circ$) tones are comparatively weak for velocities lower than 24 m s^{-1}. With increasing angle of attack the onset of transition on the suction side tends to occur further upstream, while the opposite holds true for the pressure side. The reduction of tonal noise might be ascribed to the presence of a boundary layer in a comparatively turbulent state on the suction side and late separation on the pressure side. With increasing Reynolds number, or equivalently free stream velocity for this case, separation and transition on both sides of the aerofoil tend to occur further upstream, thus allowing the growth of instability waves on the pressure side. It should further be noted that the structure of the narrowband hump changes with increasing velocity: multiple individual peaks become visible at 28 m s^{-1} and above (figure 3*b*).

3.2. *Tonal noise emission envelope*

It becomes clear from the previous discussion that tonal noise is emitted from aerofoils within specific regimes, characterized mostly by the Reynolds number and angle of attack. Many experimental observations tend to fall in between a bell-shaped envelope (figure 4), as already reported by Desquesnes *et al.* (2007), where tonal noise has often been observed (filled symbols). Data for the present study comprises relatively low Reynolds numbers ($Re = 10^5 - 2.7 \times 10^5$) and the measurement points are indicated (upright triangles). The reduction of tonal noise for lower Reynolds numbers at $\alpha = 4^\circ$ is corroborated by the data of Lowson, McAlpine & Nash (1998), Plogmann *et al.* (2013), and the low-Reynolds-number limit of Desquesnes *et al.* (2007).

When the Reynolds number is increased, separation and transition to turbulence tend to occur further upstream on both the suction and pressure sides, which is considered the cause for the suppression of tonal noise. Instead, in this regime the acoustic emissions from the aerofoil are of broadband nature (McAlpine *et al.* 1999). At zero angle of attack this limit is reached at a Reynolds number of approximately 500 000 for the NACA 0012. At the lower limit, transition will not occur upstream of the trailing edge. Instead, a laminar boundary layer and vortex shedding behind the trailing edge might result in weak or no tonal noise.

With increasing angle of attack, the separation point tends to move upstream on the suction side and downstream on the pressure side. Therefore, for an aerofoil at higher angle of attack and Reynolds number, the boundary layer on the suction side experiences transition earlier and causes broadband noise, while transition on the pressure side occurs closer to the trailing edge. At a very high angle of attack, the flow regime can better be classified as bluff-body flow, with a fully separated wake

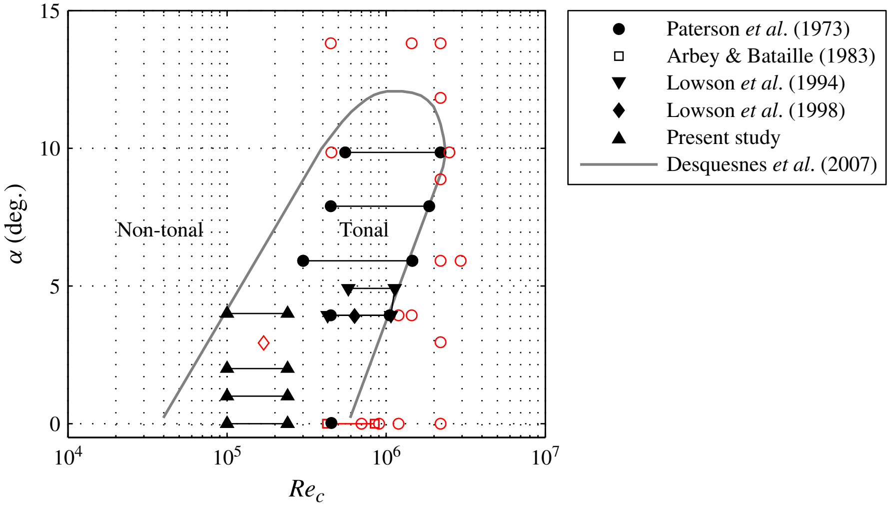

FIGURE 4. (Colour online) Tonal noise regime represented in the *Re*–α diagram. Data is relative to a NACA 0012 aerofoil. Filled (empty) symbols indicate that tonal noise is (not) observed. Solid lines between two symbols represent a range of measurements with similar results. The grey solid line indicates the tonal noise regime according to Desquesnes *et al.* (2007).

that does not interact with the aerofoil trailing edge. The high angle of attack and movement of the stagnation point implies a very favourable pressure gradient on the pressure side, delaying transition. Together with the turbulent flow condition on the suction side this justifies the absence of distinct tones.

3.3. *Scaling of tonal frequency*

Apart from the presence of multiple tones at frequencies f_n (1.2), the particular type of 'ladder' structure deserves further attention. Figure 5(*a*) shows an overview of experimental data for the NACA 0012, indicating the dominant tone frequency $f_{n_{max}}$, identified by the respective authors as a function of free stream velocity. It can be seen that the data sets of Paterson *et al.* (1973), Arbey & Bataille (1983), Nash *et al.* (1999), Takagi & Konishi (2010) and the present paper follow a $u^{0.8}$ scaling over considerable ranges of velocity or Reynolds number before a jump (transition in n) occurs, indicating a relatively coarse 'ladder' structure. A notable exception is the data set of Chong & Joseph (2012), which shows a dependency on $u^{0.8}$ scaling over very small ranges of Reynolds number only, indicating a finer 'ladder' structure. Also the data of Atobe *et al.* (2009) (not shown here) shows a different, namely constant scaling. Therefore, it appears that different types of 'ladder' structures might be associated with different mechanisms, as noted before by Tam & Ju (2012).

The difference becomes more evident when considering the data as Reynolds number against dominant tone frequency $f_{n_{max}}$, normalized by the suggested frequency scaling of Paterson *et al.* (1973) (figure 5*b*). For the present experiment, the dominant tone frequency $f_{n_{max}}$ exceeds the estimated value by factors similar to that for the data

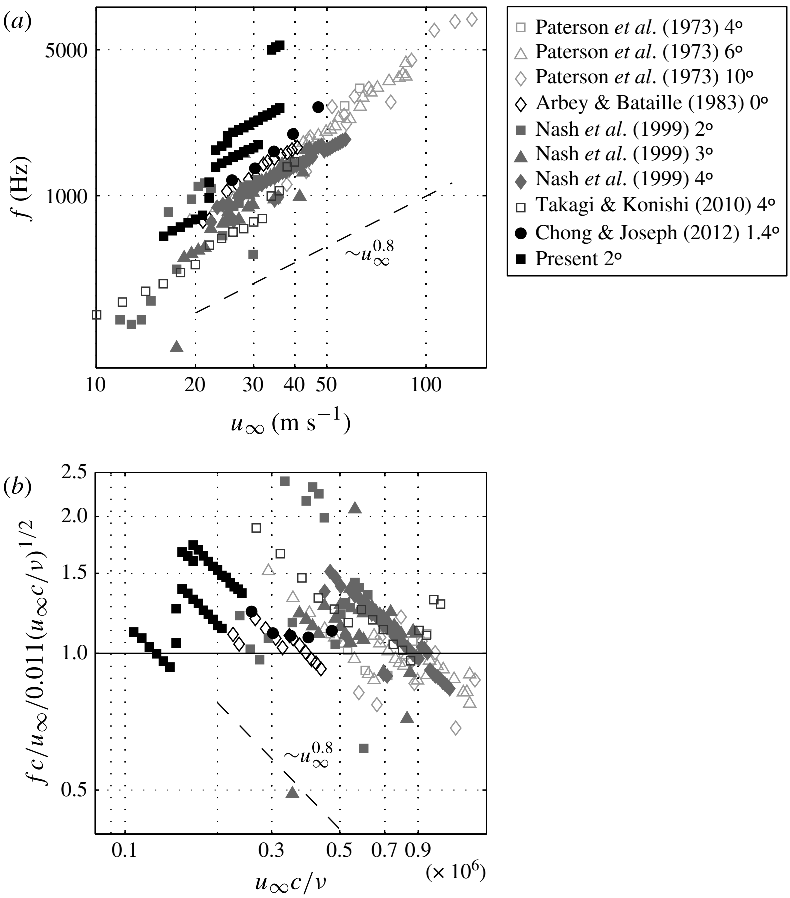

FIGURE 5. Maps of velocities and dominant tone frequency $f_{n_{max}}$ compiled from previous studies and comparison to present results in physical (*a*) and normalized units (*b*). The solid line indicate the estimation of the mean trend of the dominant tone frequency f_s (1.1) for the parameters of the different studies. The slope for the scaling of individual discrete tones f_n is also indicated ((1.2), dashed line).

of Nash *et al.* (1999) and Takagi & Konishi (2010), but also the data of Paterson *et al.* (1973) shows substantial deviations of the dominant tone frequency $f_{n_{max}}$. These deviations are not surprising, since f_s in (1.1) indicates the mean trend of the dominant tone. For the bulk of data a tendency towards higher frequencies compared to the estimated value is found for lower Reynolds numbers.

3.4. *Amplitude modulation*

The presence of multiple tones in the acoustic spectrum has been associated with an amplitude modulation through a non-stationary signal analysis by Desquesnes *et al.* (2007). Making use of a windowed short-time Fourier transform method, they investigated the acoustic pressure in the far field and observed that its amplitude modulates almost periodically. Indeed, the spectrum of a signal based on a carrier frequency $f_{n_{max}}$ and an amplitude modulation at frequency Δf reproduces the discrete tonal features as observed in the acoustic pressure spectra.

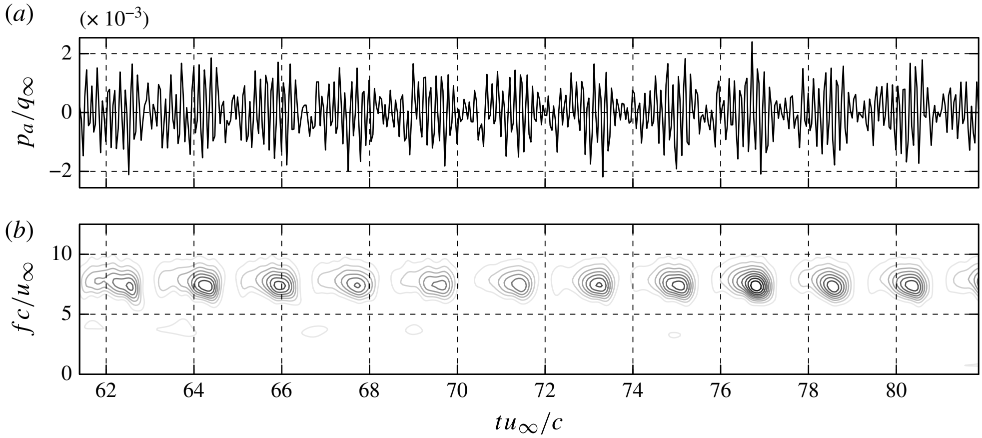

FIGURE 6. Time series (*a*) and normalized square magnitude of the wavelet coefficients (*b*) of the acoustic pressure signal, case 1.

For case 1 ($u_\infty = 24\ \text{m s}^{-1}$, $\alpha = 2^\circ$), the time series of the signal recorded by the microphone is shown in the upper part of figure 6. The period of the high-frequency oscillations in the signal is approximately 0.54 ms, while the amplitude modulates periodically with a period of approximately 7.4 ms. Introducing a normalized time reference $t^\star = tu_\infty/c$, the above-mentioned periods are equal to $\Delta t^\star = 0.13$ and $\Delta T^\star = 1.78$.

A statistical estimate of both the discrete frequency and its modulation is obtained by a wavelet decomposition of the far-field acoustic pressure. The procedure follows the recommendations given by Torrence & Compo (1998), with the Morlet wavelet chosen for this type of frequency analysis. In figure 6(*b*) the contour lines of the square modulus of the continuous wavelet transform coefficients are shown. The axes represent time and a pseudo-frequency, closely associated with the real frequency through the choice of the wavelet scale. Maxima occur centred on a horizontal line close to the dominant tone frequency $f^\star_{n_{max}} = 7.7$ (1865 Hz, see figure 2) and the regular appearance and disappearance of the peaks confirms the presence of the amplitude modulation. Matching the observation of $\Delta T^\star$ in the time series, the first modulation frequency is $\Delta f^\star = 0.56$ (135 Hz), which is equal to the frequency separation Δf observed in the acoustic spectra. In principle, this amplitude modulation is not restricted to a frequency of Δf, but can also occur at multiples of this frequency $m\Delta f$, which leads to further side peaks in the acoustic spectrum, with $m = 1, 2, \ldots$.

From the wavelet analysis, two additional features of the amplitude modulation can be observed. Firstly, the dominant tone frequency tends to decrease slightly during a single modulation cycle, which indicates that the dominant tone frequency is slightly altered along the emission cycle. Secondly, the growth of the amplitude of the oscillations before reaching the peak value appears to be less steep than the descending part.

Various researchers (Hersh & Hayden 1971; Paterson *et al.* 1973) have investigated tonal noise generation under the condition of a turbulent boundary layer on one side of the aerofoil. They observed no tonal noise when the pressure-side boundary layer was turbulent, whereas forcing transition on the suction side appeared not to have a large influence. These observations led to the conclusion that tonal noise emission is due to

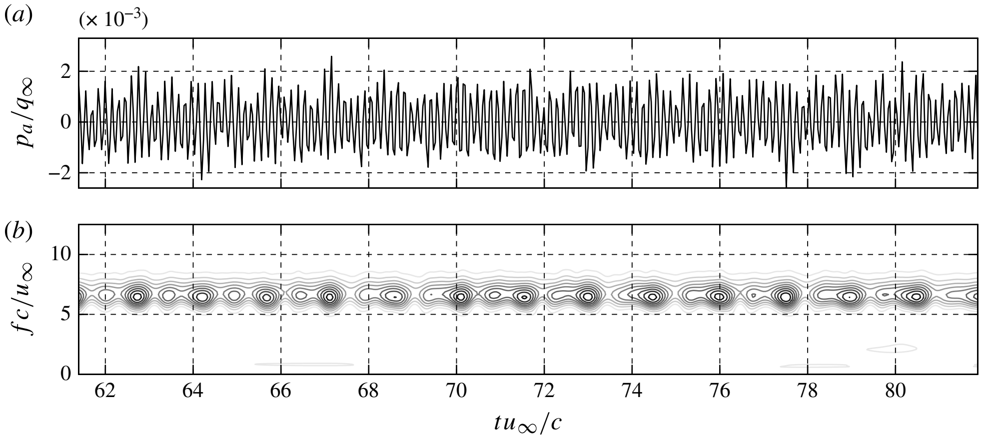

FIGURE 7. Time series (*a*) and normalized square magnitude of the wavelet coefficients (*b*) of the acoustic pressure signal, case 2 (forced transition on the suction side boundary layer).

instabilities on the pressure side. Jones & Sandberg (2011) claimed that the opposite is possible, underlining the influence of angle of attack and Reynolds number.

For the case of forced transition on the suction side of the aerofoil (24 m s^{-1}, 2°, case 2), figure 7 shows the time series and wavelet decomposition of acoustic pressure in the far field. Compared to the case where no transition is forced (figure 6, case 1) the amplitude variation, although less pronounced, is still present, while the maximum amplitude of the signal is about equal.

The wavelet analysis reveals a temporal variation of the pressure with amplitude modulation. The frequency of the dominant tone $f^\star_{n_{max}} = 6.6$ (1585 Hz) is slightly lower compared to case 1, in contrast to the modulation frequency $\Delta f^\star = 0.67$ (160 Hz). In this case the temporal variation of the amplitude is even more skewed than in the previous case: within the growth process a first peak or plateau region is observed, which will result in a harmonic component at $f^\star \approx 2\Delta f^\star$. The maximum amplitude of this secondary peak is, however, far lower in amplitude compared to the primary peak.

At a higher angle of attack (24 m s^{-1}, 4°, case 3), the flow is turbulent on the suction side. In this case only weak tones are observed (figure 2), as confirmed by the time series and wavelet decomposition of the acoustic pressure in figure 8. Overall, the amplitude of the signal remains lower compared to the tonal case at lower angle of attack (figure 6) and most energy is contained in the spectrum below $f^\star = 0.5$.

It can be concluded that the periodic amplitude modulation of the acoustic pressure is reproduced by experiments, which confirms the observations of Desquesnes *et al.* (2007) in their 2D DNS study with otherwise similar conditions and provides an explanation for the discrete tones in the spectrum. Desquesnes *et al.* (2007) explained this modulation with a vortex wake pattern bifurcation, a phase jump between the pressure fluctuations on the two sides of the trailing edge. However, there could be many reasons for such an amplitude variation in the acoustic pressure, as noted by the same authors and recently by Plogmann *et al.* (2013). Since the periodic amplitude modulation is also observed for the case of forced transition, where the relative phase of boundary layer velocity fluctuations on the two sides cannot be defined, it must be

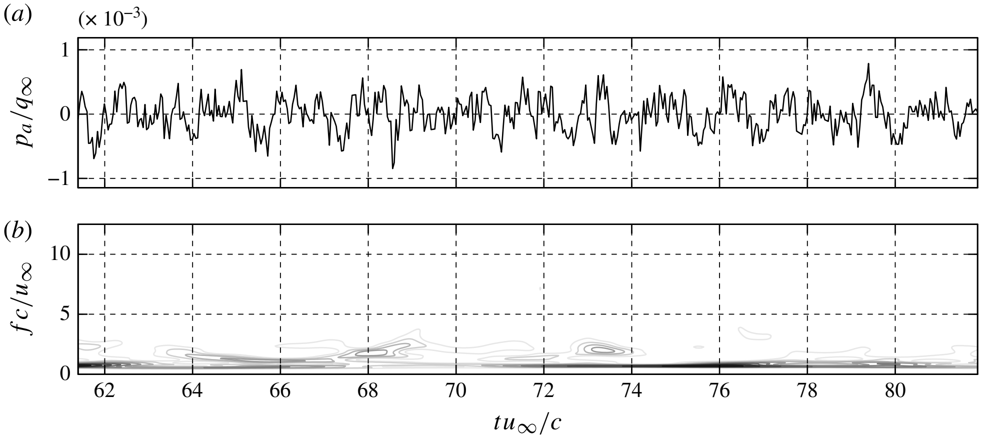

FIGURE 8. Time series (*a*) and normalized square magnitude of the wavelet coefficients (*b*) of the acoustic pressure signal, case 3.

concluded that phase modulation is not the only mechanism leading to an amplitude modulation of the acoustic pressure.

4. Flow field analysis

The instantaneous flow pattern for the cases presented here shows a number of distinctive features (figure 9), illustrated by velocity vectors overlaid on the contours of the spanwise vorticity component. For case 1, one can observe vortical structures convecting on the suction side and inducing a significant departure of the streamlines from a parallel pattern. Closer to the trailing edge the vorticity pattern appears less coherent, which indicates three-dimensional breakdown to turbulence. On the pressure side the flow appears to be laminar up to 90 % chord, where vortical structures develop due to a shear layer. An animated visualization of the vorticity field is available (See supplementary movie available at http://dx.doi.org/10.1017/jfm.2014.156). For the case of forced transition (case 2), on the suction side no large coherent structures can be observed and the boundary layer is in a turbulent state. The pressure side, however, shows similar features when compared to case 1, with a roll-up of spanwise coherent vortices close to the trailing edge. At higher angle of attack (case 3), flow on the pressure side remains laminar almost up to the trailing edge, while the boundary layer on the suction side approaches a turbulent state with an indication of large-scale turbulent bulges.

4.1. *Statistical flow description*

Based on the time-averaged properties of the velocity field the state of the boundary layer as well as its unstable modes can be inferred. For case 1 the average velocity profile on the pressure side shows an inflection point throughout the measurement domain (figure 10*a*), a necessary condition for the presence of an inviscid-type instability (Lowson *et al.* 1994). The flow is separated close to the trailing edge and roll-up of coherent vortical structures can be observed. As noted by a number of researchers (Nash *et al.* 1999; McAlpine *et al.* 1999; Desquesnes *et al.* 2007), this local flow separation is believed to be a necessary condition for tonal noise. The same authors denote this as a laminar separation bubble in cases where reattachment

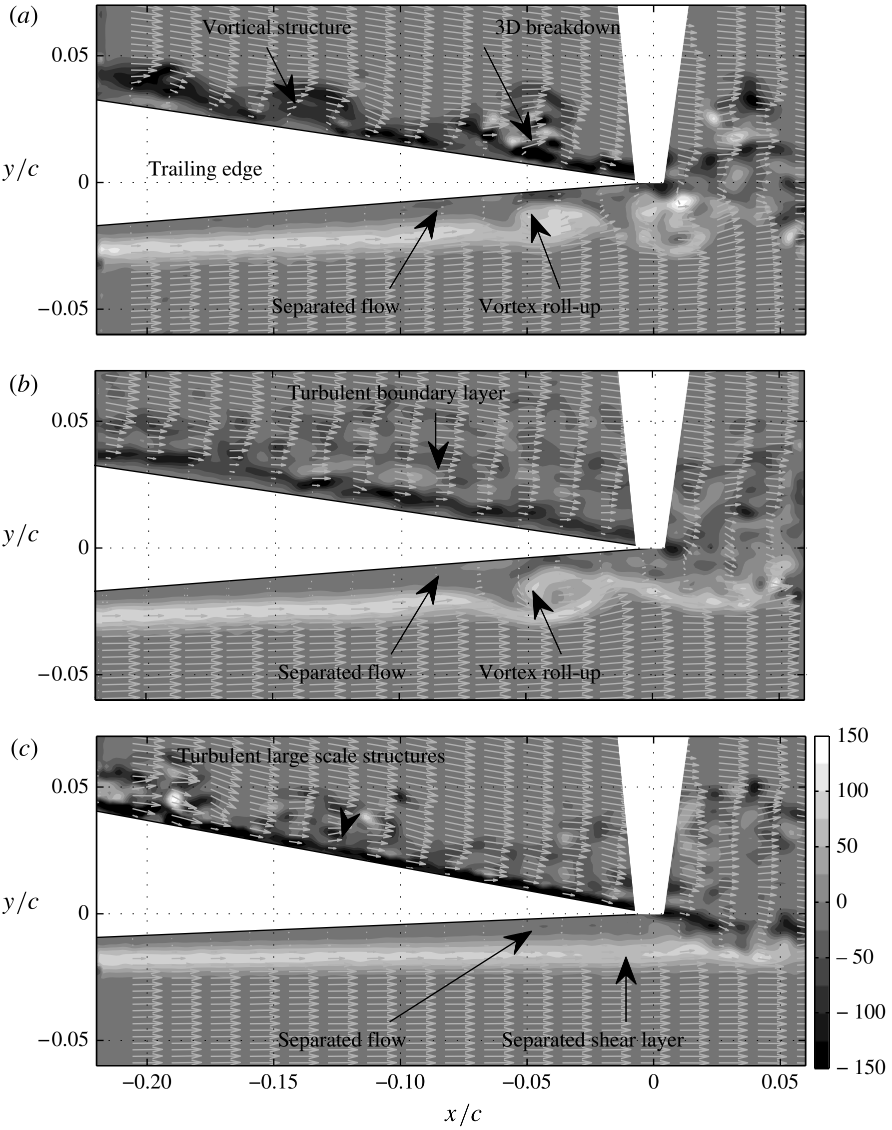

FIGURE 9. Contours of the spanwise vorticity component $\omega_z c/u_\infty$ and velocity vectors for case 1 (*a*), case 2 (*b*) and case 3 (*c*).

close to the trailing edge is observed. In the present case, the point of inflection of the mean velocity profile moves away from the wall further downstream, which is followed by an increase of the maximum reverse flow velocity. It is estimated that at the trailing edge the reverse flow attains approximately $0.1u_e$. Upstream, the time-averaged streamwise velocity fluctuations show evidence of two maxima, which can be clearly distinguished at $x_t/c = -0.05$, where an additional third peak in the upper part of the boundary layer is visible. This triple-peak structure of the streamwise velocity fluctuations is one of the features often described for cases of tonal noise emission (Nash *et al.* 1999; Desquesnes *et al.* 2007). Although the boundary layer evolves towards a turbulent state, the velocity profile at the trailing

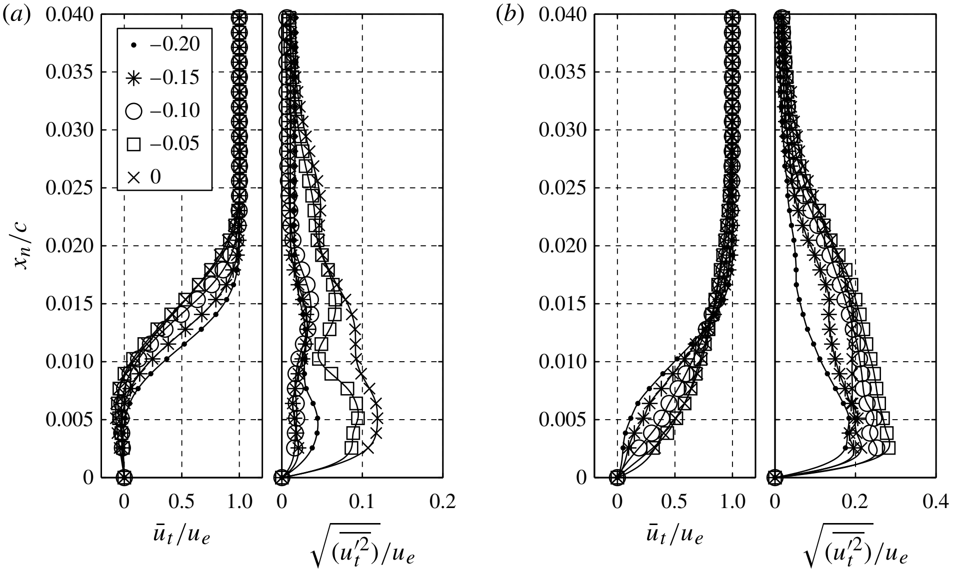

FIGURE 10. Mean (left) and root mean square fluctuations (right) of the tangential velocity component on the pressure side (*a*) and the suction side (*b*) at different x_t/c (indicated in legend), case 1.

edge is still very different from a turbulent boundary layer. The maximum value of the fluctuations attains 14 % close to the trailing edge, compared to approximately 3 % at $x_t/c < -0.15$, due to the large growth rate in this region.

Desquesnes *et al.* (2007) noted that no separation was present on the suction side in the tonal noise case, while a separation bubble was found between 18 % and 40 % chord in the non-tonal case, which falls outside the current measurement domain and cannot be verified here. The mean velocity profiles appear to recover from an earlier separation (figure 10*b*) and a separation bubble is likely to be present upstream of the observed domain. An inflection point close to the wall is found at $x_t/c = -0.2$ and -0.15, but not further downstream, indicating that the flow is attached in the aft part of the aerofoil. The profiles of velocity fluctuations reveal a double-peak structure, also reported by Desquesnes *et al.* (2007) and interpreted as evidence for the presence of a Rayleigh-type instability. It is likely that fluctuations reach a saturated state and convect past the trailing edge, which is supported by the relatively large amplitude ($u_t'/u_\infty = 0.3$) of the fluctuations at $x_t/c = -0.2$ and small variation along the streamwise coordinate.

When forcing transition on the suction side, the evolution of the mean velocity profiles on the pressure side is not seemingly altered (figure 11*a*, compare to figure 10*a*), showing a point of inflection and a region of reverse flow close to the wall. On the other hand, significant differences are present for the mean velocity fluctuations. The profiles of the first two stations in figure 11(*a*) show a single peak, suggesting that no amplified instabilities are present. Further downstream at $x_t/c = -0.1$, where values of the reverse velocity have increased in magnitude, indications of a second maximum close to the wall are present. Even further downstream this second peak increases, reaching the magnitude of the first peak at the trailing edge. No clear triple-peak structure is evident for this case upstream of

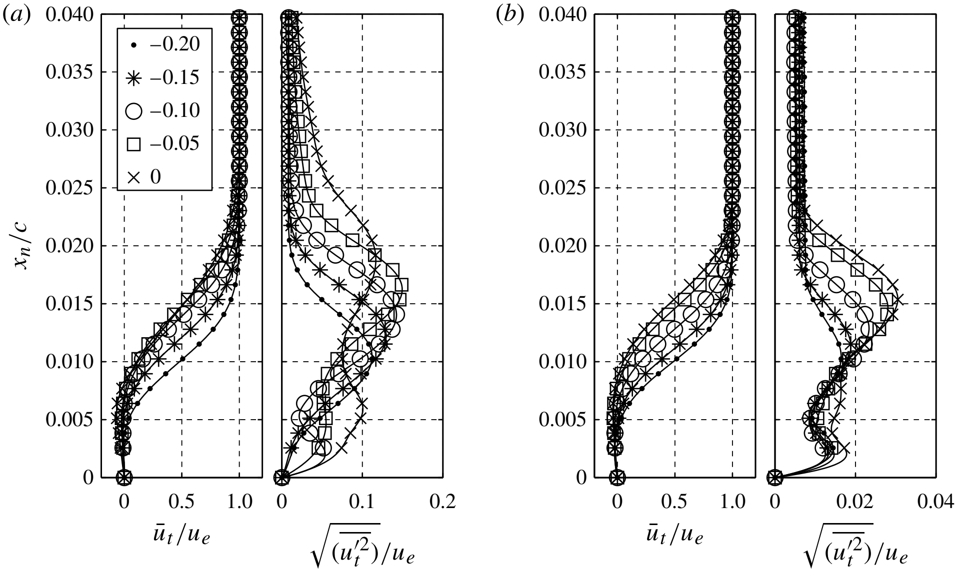

FIGURE 11. Mean (left) and root mean square fluctuations (right) of the tangential velocity component on the pressure side for case 2 (*a*) and case 3 (*b*) at different x_t/c (indicated in legend).

the trailing edge. This suggests that a triple-peak structure is not a necessary feature in the case of tonal emission, as reported by Nash *et al.* (1999).

In the absence of strong tones (case 3), the mean tangential velocity profiles on the pressure side (figure 11*b*) also reveal a region of reverse flow, yet with a slightly lower peak. A profound difference with respect to case 2 is found in terms of turbulence levels. With a maximum value below 3 % up to the trailing edge, the fluctuations in this case are relatively small due to the absence of larger amplitude vortical structures. The scenario here is that the boundary layer undergoes laminar separation close to the trailing edge and the growth of the instabilities is delayed with respect to lower angles of attack (case 2, figure 9). This is consistent with a shift of the stagnation point towards the suction side on the aerofoil nose and a shift downstream of the region of favourable pressure gradient.

4.2. *Linear stability analysis*

Arbey & Bataille (1983) ascribed the narrowband contribution of the acoustic spectrum to the diffraction at the trailing edge of the pressure perturbations induced by growing instabilities, since they found by linear stability analysis that the unstable mode with the largest growth rate occurs at a frequency close to the broadband centre frequency in the acoustic spectrum.

Thereafter, spatial linear stability analysis has been applied by a number of researchers (McAlpine *et al.* 1999; Nash *et al.* 1999; Desquesnes *et al.* 2007; Kingan & Pearse 2009; Jones & Sandberg 2011; Ikeda *et al.* 2012; Plogmann *et al.* 2013) for identification of the most amplified modes and was already suggested by Tam (1974). In most cases this frequency is close to the dominant tone frequency, leading to the belief that one relates to the other (McAlpine *et al.* 1999; Desquesnes *et al.* 2007). Moreover, Boutilier & Yarusevych (2012) report that the maximum growth

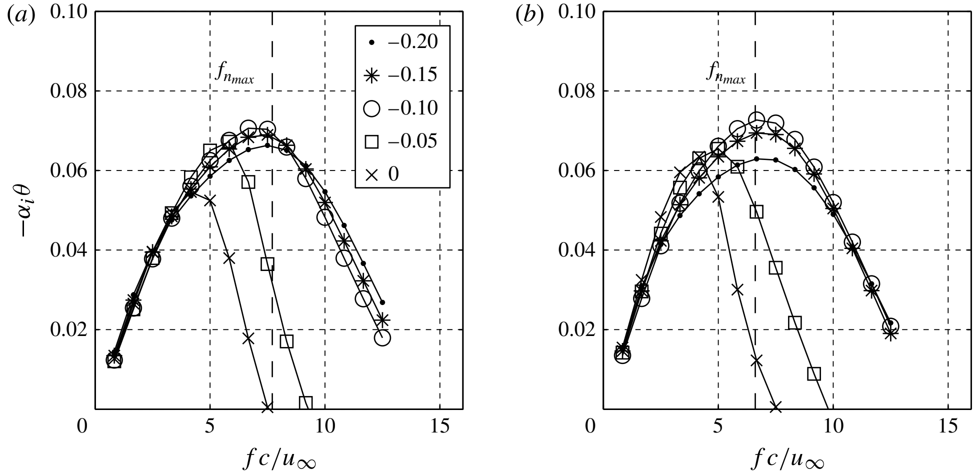

FIGURE 12. Spatial growth rate determined from linear stability analysis based on pressure-side mean velocity profiles for case 1 (*a*) and case 2 (*b*) at different x_t/c (indicated in legend). Dashed line indicates the dominant tonal frequency observed in the acoustic spectra.

rate indicates the most amplified disturbances in the shear layer, and thus the roll-up frequency. This assumption has recently been challenged by Jones & Sandberg (2011), who investigated the hydrodynamic instability based on a 2D DNS.

Based on the time-averaged velocity profiles (§ 4.1), the growth rates for a range of frequencies have been obtained by solving the Orr–Sommerfeld equation (4.1) (van Ingen & Kotsonis 2011). The disturbances in the boundary layer can be described by a stream function $\Psi(y) = \Phi(y)\mathrm{e}^{\mathrm{i}(\alpha x-\omega t)}$, where the eigenfuction $\Phi(y) = \alpha_0/2 + \sum_{n=1}^{N} \alpha_n T_n(y)$ can be expressed in a series of Chebychev polynomials $T_n(y)$ and $u(y)$ is the function describing the streamwise velocity component distribution as a function of the wall-normal coordinate:

$$\left[\left(\frac{\mathrm{d}^2}{\mathrm{d}y^2}-\alpha^2\right)^2 - \mathrm{i}Re\,(\alpha u-\omega)\left(\frac{\mathrm{d}^2}{\mathrm{d}y^2}-\alpha^2\right) - \alpha u''\right]\Phi = 0. \tag{4.1}$$

An estimation for $u(y)$ is based on the time average of the measured velocity fields. Fourfold integration over y with an appropriate choice of boundary conditions and expansion of the eigenfunction yields a system of equations that can be solved for α with given frequency ω and Reynolds number Re as a function of the streamwise coordinate. Modes are unstable if the imaginary part of the wavenumber, referred to as growth rate, $\mathrm{Im}\{\alpha\} < 0$.

Figure 12(*a*) shows the results for different locations along the chord on the pressure side for case 1. Note that the local boundary layer momentum thickness θ is selected as characteristic length scale for dimensionless parameters. As observed in previous studies, the maxima indicate that the frequency associated with the largest growth rate is close to the frequency of the dominant tone (dashed line, $f^\star_{n_{max}} = 7.7$).

For the case of forced transition on the suction side (case 2), figure 12(*b*) shows similar results. Away from the trailing edge ($x_t/c < -0.1$) the frequency associated with the maximum growth rate is close to that of the dominant tone observed in the spectrum of acoustic pressure (dashed line, $f^{\star}_{n_{max}} = 6.6$). Closer to the trailing edge this frequency deviates more. It should be noted that the assumption of parallel flow and small disturbances with linear growth does not apply to the region where large vortices appear. This, however, is the case close to the trailing edge, providing an explanation for the deviations.

It might be argued about the coupling of the flow and the importance of instabilities on the two sides of the aerofoil. Most likely, the answer for a symmetric profile such as the NACA 0012 depends on the angle of attack and Reynolds number under consideration. At zero incidence and perfectly symmetric conditions, instabilities developed on the two sides of the aerofoil must be equally significant for tonal noise generation. With increasing angle of attack the flow becomes asymmetric and separation tends to occur further upstream on the suction side than on the pressure side. As a result, the pressure-side boundary layer features separation close to the trailing edge in combination with large growth rates, whereas vortical structures on the suction side appear merely to convect (case 1).

4.3. *Time-resolved analysis*

An effective way to visualize the properties of the vortical structures is by referring to the contours of the wall-normal velocity component, in this case approximated by the transverse velocity component. Figure 13(*a*) illustrates a sequence of contours for the aerofoil at 2° incidence and 24 m s^{-1} (case 1). The time separation between two consecutive images is $\sim$167 μs, equivalent to a measurement frequency of 6 kHz. The spatial pattern of velocity fluctuations on the suction side predominantly convects downstream, while on the pressure side the amplitude grows over the aft 10 mm and ultimately approaches that of the suction side near the trailing edge. The wavelength here is about half that of the suction side and the convective velocity is lower.

The transverse velocity component shows only a small difference in phase at the trailing edge. As a result, the transverse fluctuations past the trailing edge appear further amplified. This constructive interference is not a stable situation and the phase difference varies over time, yielding the modulation effect of the dipolar emissions from the trailing edge, as discussed by Desquesnes *et al.* (2007).

When the transition on the suction side (figure 13*b*) is forced, the boundary layer most likely does not undergo separation and develops along the aerofoil in the turbulent regime. As a result, no coherently convecting vortical structures are visible. Due to the absence of these structures the relative phase of the velocity fluctuations on the two sides cannot be defined. This observation excludes a periodic phase modulation of velocity fluctuations (Desquesnes *et al.* 2007) being the only possible reason for an amplitude modulation of the acoustic pressure, as also noted recently by Plogmann *et al.* (2013). Instead, a different explanation for the amplitude modulation must be sought.

When the angle of attack is further increased to 4° (figure 13*c*) the separated flow on the suction side undergoes transition to turbulence before reaching the trailing edge. However, as commented on earlier, evidence of larger scale convecting turbulent bulges is present. On the pressure side the region of favourable pressure gradient moves further downstream and no convecting instabilities are visible upstream of the trailing edge. The overall comparison of the three cases presented here underlines the importance of pressure side boundary layer instabilities and their rapid growth for tonal noise emission at this Reynolds number.

The coherent structures visible in figure 13 convect downstream, as demonstrated for case 1 by the space–time contours of the wall-normal velocity component sampled

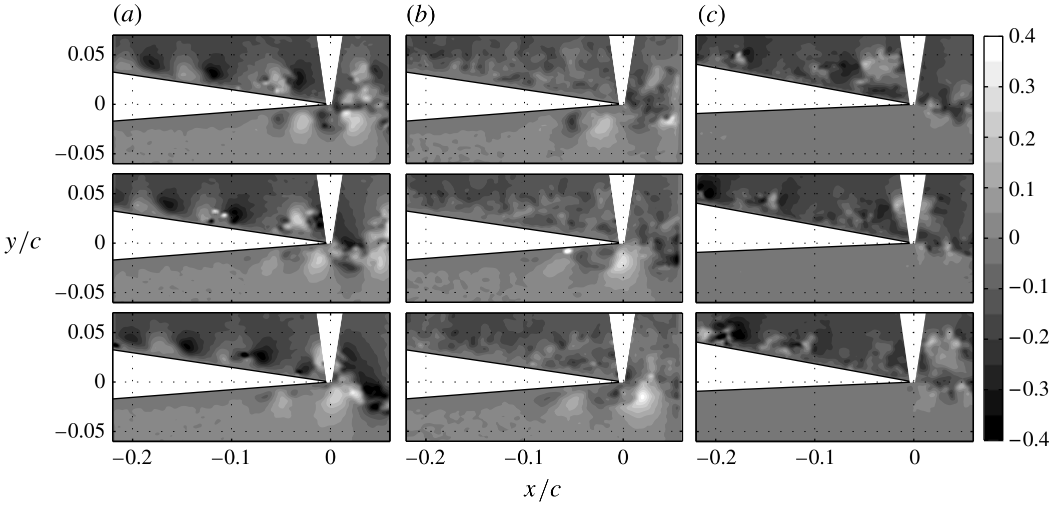

FIGURE 13. Sequences of three instantaneous velocity fields (6 kHz): case 1 (*a*), case 2 with forced transition on the suction side (*b*), and case 3 (*c*). Contour levels for the transverse velocity component v/u_∞ are indicated.

along a line parallel to the surface of the aerofoil in figure 14. On the suction side the amplitude of the signal remains comparatively constant over the measurement domain (figure 14*a*) when compared to the pressure side (figure 14*b*), but close to the trailing edge the signal becomes less coherent due to breakdown of the large-scale structures to turbulence. The convection velocity of the large-scale structures is indicated by the slope of the dashed lines following the extrema in the diagram. On the suction side this convection velocity attains a value ($0.64u_\infty$, 15.4 m s^{-1}) approximately twice that on the pressure side ($0.32u_\infty$, 7.7 m s^{-1}). For free stream velocities other than that presented here, these ratios remain relatively constant. Case 2 shows a similar picture (figure 14*c*) and convection velocity on the pressure side ($0.31u_\infty$, 7.5 m s^{-1}), but an earlier onset of transition.

Figures 15(*a*) and 15(*b*) show a comparison of the power spectra for the wall-normal velocity component at a point close to the trailing edge ($x_t = -1.1$ mm, $x_n = 1.9$ mm) for all three cases on the pressure and suction sides, respectively. The average periodogram method (Welch 1967) is applied to compute the power spectra with segments of 512 samples and an overlap of 50 %, where the Hamming window is applied to each segment (Harris 1978). This procedure results in a frequency resolution of 11.7 Hz. For case 1 the most striking feature on the suction side (figure 15*a*) is the dominant peak at $f^{\star}_{n_{max}} = 7.7$ (1865 Hz) with symmetrically arranged side peaks, which will be elaborated on in § 4.4. On the pressure side (figure 15*b*) similar frequencies and side peak structure are present. When compared to the suction side, peaks reach similar levels, while the broadband component is smaller by 2–5 dB due to the earlier stage of transition. Forcing transition on the suction side of the aerofoil (case 2) leaves only the indication of a peak at a lower frequency ($f^{\star}_{n_{max}} = 6.6$, 1585 Hz), matching that of the maximum peak on the pressure side, but with a similar side peak structure as observed for case 1. This marked difference suggests that the remaining frequency peak on the suction side is due to the influence of

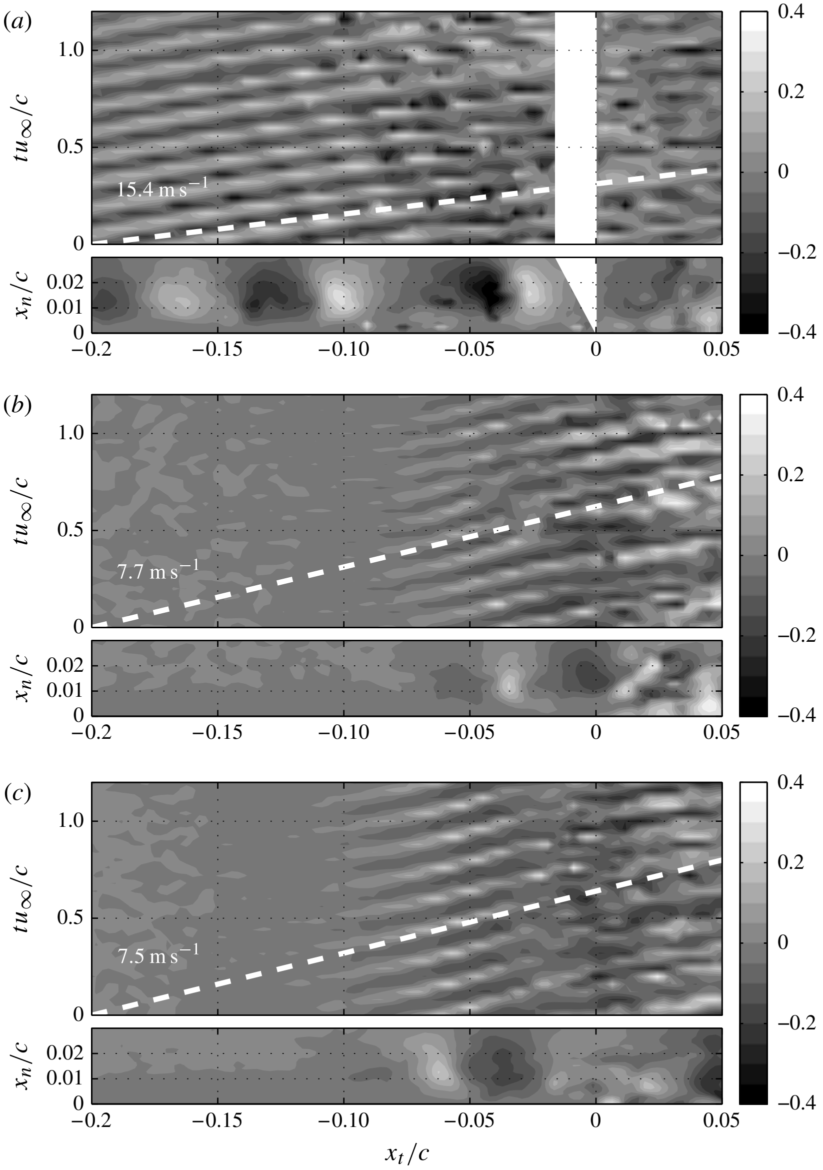

FIGURE 14. Contours of the wall-normal velocity component u_n/u_∞ on the suction side (*a*) and the pressure side (*b*) for case 1 and the pressure side for case 2 (*c*) in the space–time domain sampled along a line at $x_n = 1.3$ mm (top of sub-figure) and in space at $t = 0$ (bottom of sub-figure). Dashed line indicates the average convection velocity based on wavenumber–frequency analysis (figure 16).

shedding from the pressure side. Note that the second largest peak close to $f^\star = 12$ is due to aliasing. For the aerofoil at larger angle of attack (case 3) the flow field at the sampling location on the pressure side does not show large amplitude fluctuations (figure 13*c*). Therefore, the fluctuation levels are very low when compared to the fluctuations in the transitional cases (cases 1 and 2) and the levels found approach

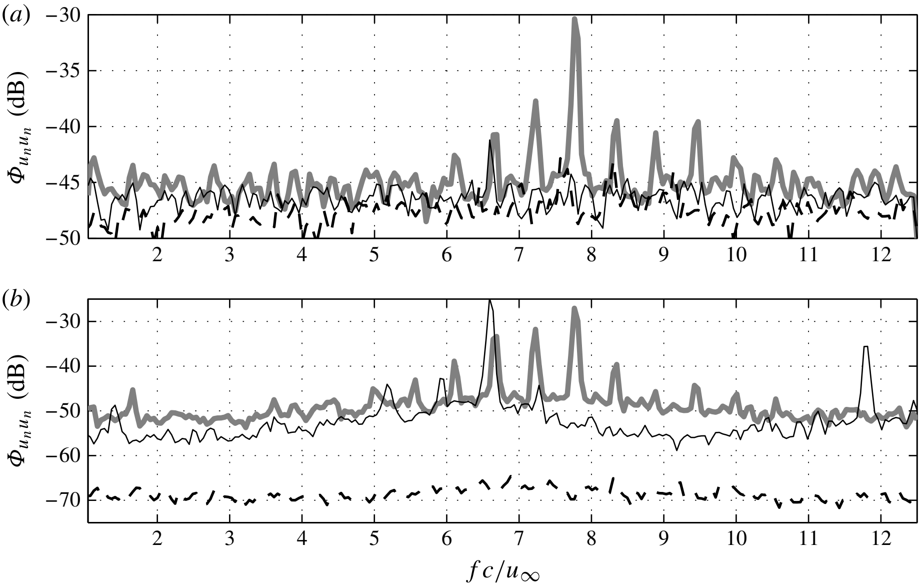

FIGURE 15. Spectra of the wall-normal velocity component on the suction side (*a*) and the pressure side (*b*) at $x_t = -1.1$ mm, $x_n = 1.9$ mm for case 1 (thick grey lines), case 2 (thin black lines), and case 3 (black dashed).

the experimental error associated with planar PIV. On the suction side, indications of weaker peaks at frequencies similar to those of case 1 are found.

A representation of the wall-normal velocity fluctuations along a line parallel to the surface (figure 14) in wavenumber–frequency space shows maxima (figure 16) at the same frequencies as the power spectra (figure 15). The wavenumber–frequency decompositions are obtained by following a similar approach to the average periodogram method for power spectra (Welch 1967), but based on the two-dimensional Fourier transform over time and space, with Hamming windows (Harris 1978) applied over both dimensions. Energy content at positive wavenumbers indicates downstream propagating waves, while negative wavenumbers represent upstream propagation. For both the suction side (figure 16*a*) and the pressure side (figure 16*b*) the maxima associated with the tonal noise are located in the first quadrant (positive wavenumbers). As anticipated, the convection velocity (grey solid line) on the suction side attains about twice the value on the pressure side under the assumption of constant convection velocity over the domain considered here. The wavelength relating this convection velocity to the tonal frequency indicates the length scale of the associated flow structures, in this case 8.3 mm ($\lambda/c = 0.083$) and 4.1 mm ($\lambda/c = 0.041$) on the suction side and pressure side, respectively. These length scales match the wavelength of the wall-normal velocity fluctuations in figure 14 for case 1. Maxima in the fourth quadrant (negative wavenumbers) are due to aliasing, and resemble spurious, upstream propagating waves.

4.4. *Amplitude modulation of the source*

The presence of side peaks in the acoustic power spectrum for the case of forced transition (case 2) indicates that a variation in phase shift for the fluctuations on the

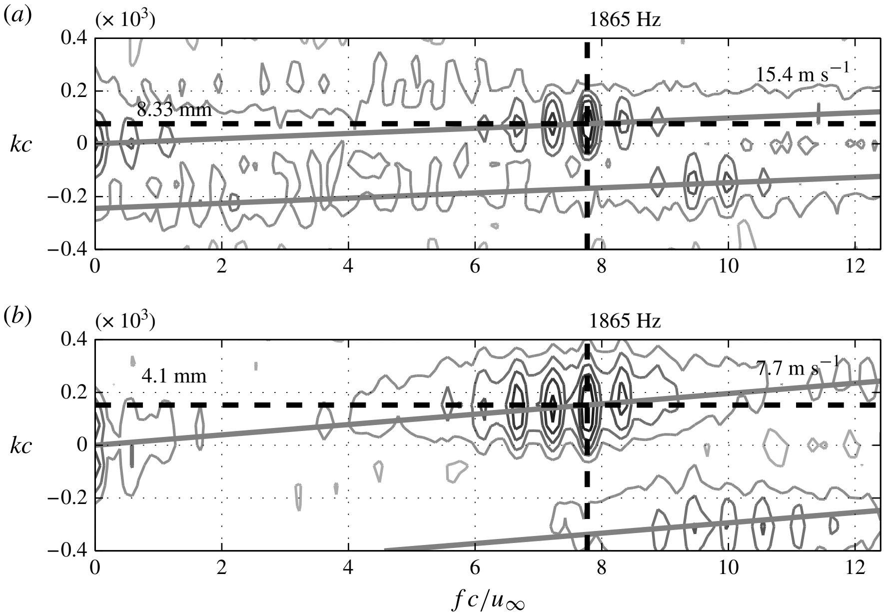

FIGURE 16. Wavenumber–frequency spectra of the wall-normal velocity component (contour lines, grey to black) on the suction side (*a*) and the pressure side (*b*), $x_n = 1.2$ mm, case 1. Also indicated are the convection velocity (solid line), dominant tone frequency and the corresponding wavelength.

two sides of the aerofoil cannot be the only reason for periodic amplitude modulation. An alternative explanation is sought for by inspection of the spectral characteristics of the source field.

For the clean case (case 1), the power spectrum of the acoustic pressure (figure 17*c*) shows a dominant tone at $f^{\star}_{n_{max}} = 7.7$ (1865 Hz) and a modulation frequency $\Delta f^{\star} = 0.56$ (135 Hz), explaining the occurrence of multiple tones as side peaks of a centre frequency $f_{n_{max}}$ (§ 3.4).

Comparing the velocity spectra (figure 17*a*) to the acoustic spectrum, similar features are found, including a slight asymmetry of the side peaks, which reflects a similar distribution of energy when compared to the acoustic spectrum. On the suction side the velocity spectra at all locations are very similar, confirming the convection of instability waves without significant growth or decay. A different situation arises on the pressure side, where velocity fluctuations undergo amplification in the vicinity of the trailing edge. The similarity of these spectra suggests a similar modulation of the velocity amplitude in the source region, which in turn implies a modulation of the wall pressure. In view of diffraction theory (Amiet 1976), relating wall pressure fluctuations to the far-field acoustic pressure, a periodic amplitude modulation of the convecting instabilities can provide an explanation for the appearance of multiple tones.

To investigate the amplitude modulation of the wall-normal velocity component at a point near the trailing edge, the signal is decomposed using wavelet analysis. Figure 18 presents a time series of the wall-normal velocity component and its wavelet decomposition ($x_t/c = -0.05$, $x_n/c = 0.02$) for case 1 (24 m s^{-1}, $\alpha = 2°$) on the pressure side. The temporal diagram shows strong similarities to the acoustic

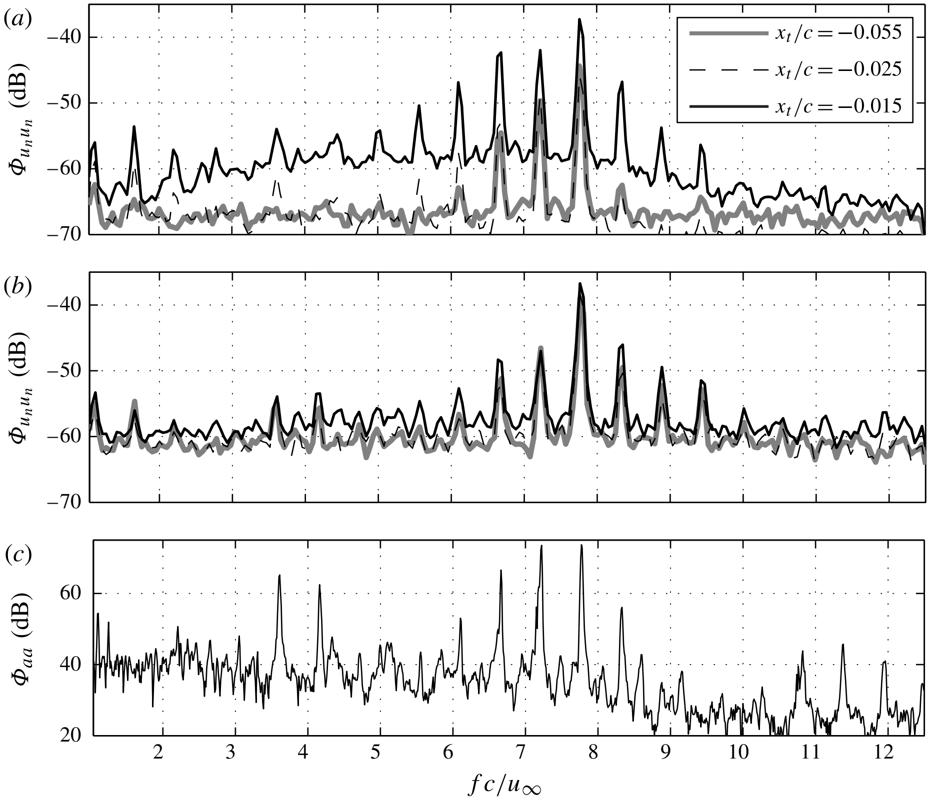

FIGURE 17. Spectra of the wall-normal velocity component on the pressure side (*a*) and the suction side (*b*) at $x_n/c = 0.038$ and spectrum of the acoustic pressure (*c*), case 1.

pressure (figure 6) in terms of amplitude modulation and its period. The wavelet decomposition shows more clearly the energy contained at a crest centred at $f^\star = 7.7$ (1865 Hz), with a modulation frequency of approximately $\Delta f^\star = 0.56$ (135 Hz). Closer examination reveals an incidentally occurring double-peak structure at the same centre frequency, which might be explained by a combination of higher harmonics of the base modulation frequency $\Delta f^\star$. The presence of the almost periodic amplitude modulation strengthens the hypothesis regarding the important role of convecting instabilities on the noise generation process.

The velocity signal on the suction side does not follow the features of the acoustic signal as closely (figure 19). As became clear from the interpretation of the flow statistics in § 4.1, the mean square fluctuating velocity is slightly larger on the suction side, and a similar but less coherent amplitude modulation is present in the time signal. The wavelet analysis confirms the presence of periodic amplitude modulation, but with the already mentioned double-peak structure being far more pronounced on this side.

Considering contours of vorticity there is a striking difference in the flow structure between the high- and low-amplitude phase of the noise generation process (figure 20). While in the high-amplitude case distinct vortices are present in the boundary layer on both sides, in the situation with weak tones a separated shear layer is observed without large vortical structures on the pressure side.

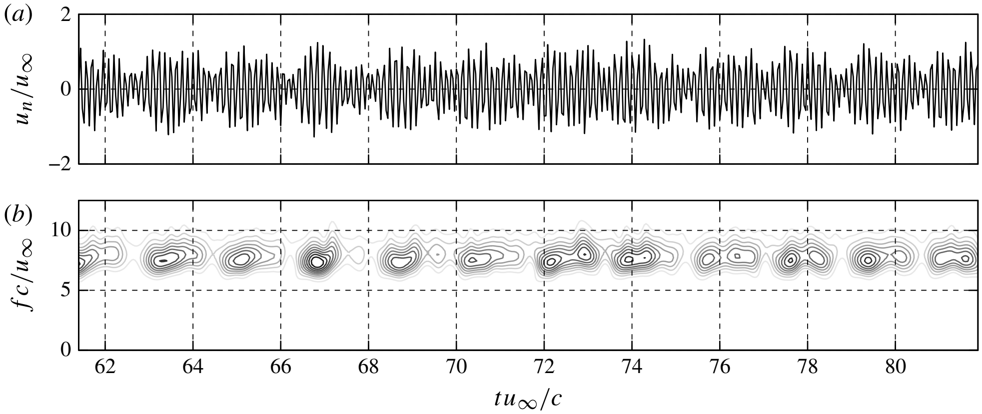

FIGURE 18. Time series (*a*) and normalized square magnitude of the wavelet coefficients (*b*) of the wall-normal velocity component on the pressure side, $x_t/c = -0.05, x_n/c = 0.02$, case 1.

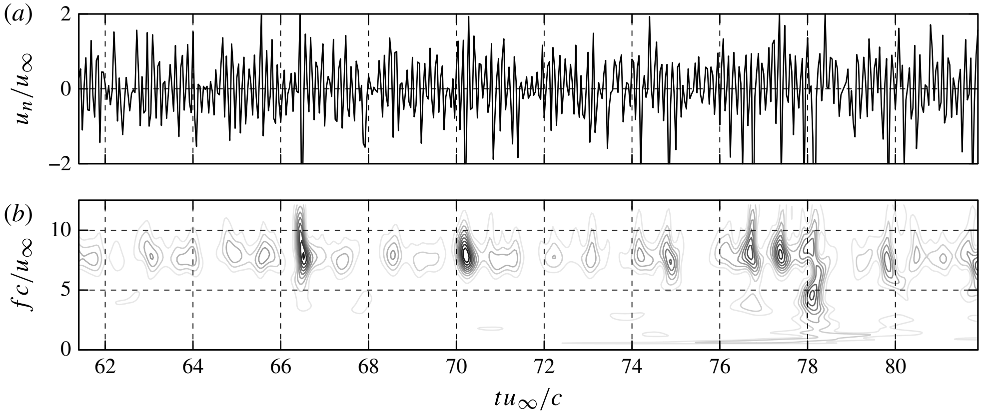

FIGURE 19. Time series (*a*) and normalized square magnitude of the wavelet coefficients (*b*) of the wall-normal velocity component on the suction side, $x_t/c = -0.05, x_n/c = 0.02$, case 1.

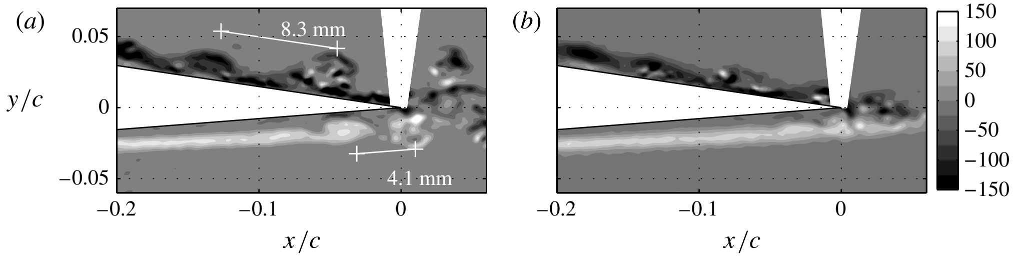

FIGURE 20. Contours of vorticity during the period of high-amplitude (*a*) and low-amplitude (*b*) noise emission, case 1. For the high-amplitude case the characteristic wavelength determined based on the dominant tone frequency and convection velocity (compare figure 16) is indicated.

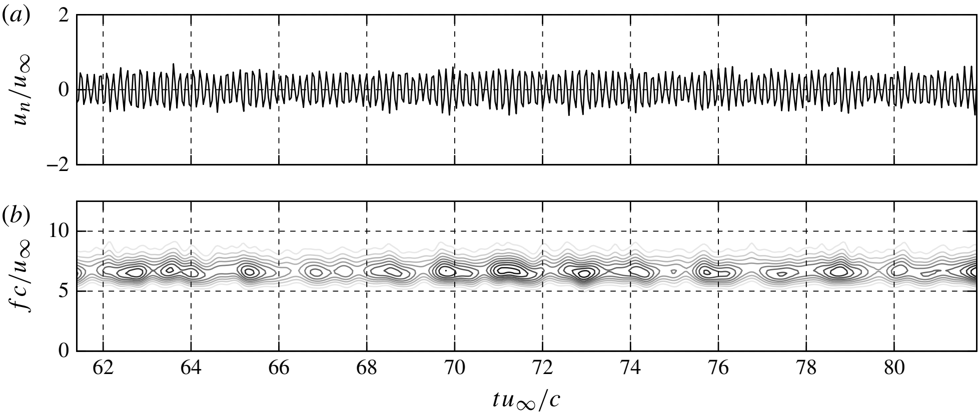

FIGURE 21. Time series (*a*) and normalized square magnitude of the wavelet coefficients (*b*) of the wall-normal velocity component on the pressure side, $x_t/c = -0.05$, $x_n/c = 0.02$, case 2.

Interestingly, even with forced transition on the suction side, multiple tones remain present (case 2). If the hypothesis holds true that this is due to a periodic amplitude modulation of instabilities, then this periodic amplitude modulation should also be present for the velocity components on the pressure side. The time series of the wall-normal velocity component confirms this amplitude modulation (figure 21), although less pronounced compared to the clean configuration (case 1, figure 18). The wavelet decomposition reveals the amplitude modulation of a base signal at a slightly lower frequency $f^\star_{n_{max}} = 6.6$ (1585 Hz) with a modulation frequency of approximately $\Delta f^\star = 0.67$ (160 Hz), as observed in the acoustic signal (figure 7).

In summary, these results indicate that in both cases examined here a substantial, periodic amplitude modulation of the velocity fluctuations on the pressure side is present, which introduces frequencies matching those of the tones. This periodic amplitude modulation of both the convecting hydrodynamic fluctuations and acoustic pressure leads to the tonal peaks present in the acoustic spectrum. Even in the case of a single-sided transitional boundary layer, the amplitude modulation is present, invoking a very similar effect and acoustic spectrum. However, a slight shift of the main frequency is observed, which might be due to a change in the mean flow and the consequent stability characteristics on the pressure side.

A method for combining simultaneous PIV and acoustic measurements for the analysis of an aeroacoustics source has been described by Henning *et al.* (2008) and is based on the cross-correlation between a near-field quantity measured by PIV at position $\boldsymbol{y}$ and time t and the acoustic pressure $p'(\boldsymbol{x}, t)$ at the position of one microphone $\boldsymbol{x}$. The normalized cross-correlation function for a time shift τ is defined in (4.2), where $\langle\cdot\rangle$ denotes a time average.

$$R_{\Phi,p'}(\boldsymbol{x}, \boldsymbol{y}, \tau) = \frac{\langle \Phi(\boldsymbol{y}, t)\, p'(\boldsymbol{x}, t+\tau)\rangle}{\sqrt{\langle \Phi^2(\boldsymbol{y}, t)\rangle \langle p'^2(\boldsymbol{x}, t)\rangle}}. \tag{4.2}$$

Figure 22(*a*) shows the distribution of the cross-correlation coefficient for $\tau = 0$ (case 1), where the time shift has been corrected for the propagation time between the trailing edge and the location of the microphone. The result is similar to that

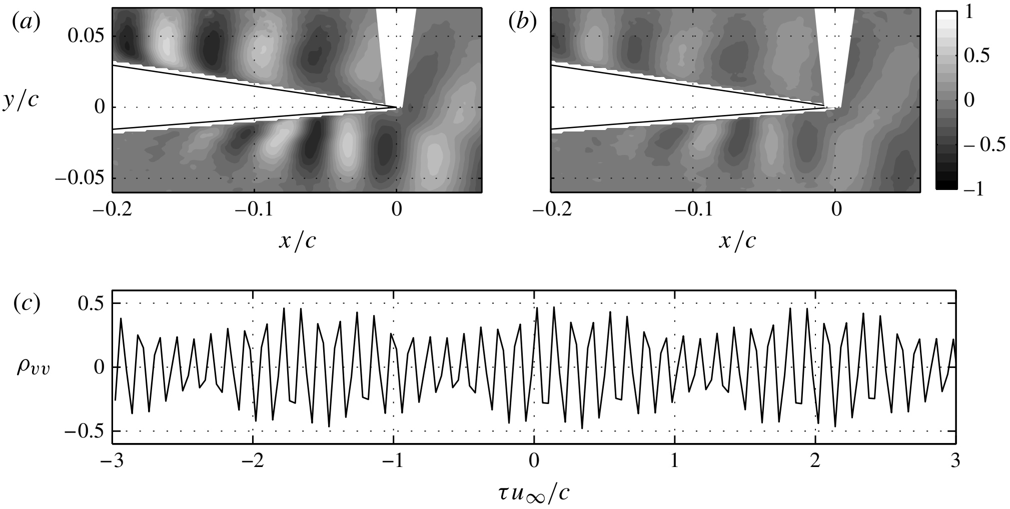

FIGURE 22. Contours of the correlation coefficient (4.2) between the transverse velocity component and the acoustic pressure signal for $\tau = 0$ (*a*) and $\tau = 1/2\Delta f$ (*b*), case 1. Time series of the correlation coefficient between the transverse velocity sampled at point $x/c = -0.02$, $y/c = 0.04$ and the acoustic pressure signal.

observed in the instantaneous velocity fields (figure 13*a*), with an alternating pattern of positive and negative values, also shown by Nakano *et al.* (2006). Since the acoustic pressure is dominated by the component at the dominant tone frequency, the frequency at which the convecting vortical structures pass the trailing edge in the source field must be associated with and equal to this dominant tone frequency. It can be noted that the contours of correlation coefficient show comparatively high values even outside the domain typically defined as the boundary layer. This result can be understood when considering the high circulation connected to strong vortices in the boundary layer, whose presence can also be felt in the free stream, and the definition of the causality correlation, involving a normalization of the correlation function with the mean of the local velocity fluctuations (see (4.2)). The correlation coefficient is an indication of the ratio of the correlated part of the signal with respect to its overall energy; therefore its values in the free stream can be high compared to the boundary layer, where the correlation coefficient can deteriorate due to 3D vortex breakdown and consequent uncorrelated turbulence.

With a time shift $\tau = 1/(2\Delta f)$, equal to half the modulation period, the correlation coefficient shows the same structure and frequency, but substantially lower magnitudes. This indicates that both quantities show modulation at a similar frequency, also confirmed by the strongly periodically modulated nature of the correlation coefficient at point $x/c = -0.02$, $y/c = 0.04$ as a function of time separation τ (figure 22*c*). The periodic modulation of the correlation coefficient indicates that it is not only pure amplitude modulation of the convecting instabilities, but that other effects such as breakdown to turbulence accentuate this effect, effectively reducing the correlation coefficient. Thus, causality correlation supports the hypothesis that the periodically modulated convecting instabilities observed in the flow field on both sides of the aerofoil upstream of the trailing edge are related to the noise generation. Wake instability as the sole mechanism for tonal noise generation can be excluded for the cases investigated here.

Desquesnes *et al.* (2007) suggested a phase modulation between the velocity fluctuations on the two sides of the aerofoil, including a secondary feedback loop on the suction side, as a possible cause, and as a result a varying intensity of the scattered acoustic waves. The results of the transient analysis suggest (figure 18) a periodic amplitude modulation of the convecting instability waves as an alternative explanation. The periodic amplitude modulation of the acoustic waves explains the presence of multiple tones in the spectrum, but the question with respect to its physical cause and the frequency selection mechanism remains. In view of the feedback loop hypothesis, which has been proclaimed by a number of researchers in the past (Arbey & Bataille 1983; Desquesnes *et al.* 2007) and recently demonstrated in an experimental study by Plogmann *et al.* (2013), the periodic amplitude modulation of the velocity fluctuations found in the present study might be described as follows:

(*a*) Wall pressure fluctuations in the boundary layer induced by the presence of vortical structures scatter at the trailing edge in the form of acoustic waves.
(*b*) These acoustic waves propagate upstream and influence the initial amplitude of perturbations in the receptivity region, causing a periodic modulation.
(*c*) Amplification of the modulated perturbations and convection of vortical structures towards the trailing edge.

5. Conclusion

Combined high-speed PIV and acoustic measurements have been performed to investigate the tonal noise generation and the underlying aeroacoustic source mechanism on a NACA 0012 aerofoil at low Reynolds numbers. Tonal noise is observed for the entire range of parameters considered in this study, but is comparatively weak at the higher angle of attack ($\alpha = 4^\circ$) and low Reynolds numbers.

The frequency scaling of individual tones with free stream velocity shows similar scaling ($f_n \sim u_\infty^{0.8}$) as reported in the preceding studies of Paterson *et al.* (1973), Arbey & Bataille (1983), Nash *et al.* (1999) and Takagi & Konishi (2010). Amongst these tones the dominant one is found to follow this scaling over substantial ranges of Reynolds number before transition occurs. Substantial differences appear in comparison to the data of Atobe *et al.* (2009), who observed a constant scaling in a resonant environment, and Chong & Joseph (2012). In the latter case an almost continuous transition of the dominant tone frequency (following $f_s \sim u_\infty^{1.5}$) was observed. The reason for these differences in the details of the 'ladder' structure remains in parts unclear.

For the cases presented here, and with respect to the nature of tones in the spectrum, temporal and spectral analysis of the experimentally acquired data confirm the presence of a periodic amplitude modulation for the acoustic pressure, already observed by Desquesnes *et al.* (2007) in a DNS study. Wavelet decomposition of the signal reveals modulation frequencies of $m\Delta f$, with $m = 1, 2, \ldots,$ related to the occurrence of side peaks in the power spectrum with frequency separation $2m\Delta f$.

It is demonstrated by spatio-temporal analysis of the PIV data and causality correlation with the acoustic pressure that the dominant tone frequency $f_{n_{max}}$ is equal to the frequency at which vortical structures pass the trailing edge. Similar to the findings of previous studies, this frequency is found by linear stability analysis to be close to the frequency of the most amplified waves. For the parameter and boundary conditions of the present experiment, and based on this direct observation and correlation, the hypothesis of wake instability as the mechanism for tonal noise generation (Tam 1974) can be excluded.

Vortical structures on the pressure side in the vicinity of the trailing edge appear to be substantially more coherent than their counterparts on the suction side, where 3D breakdown is observed. Considering the importance of spanwise coherence for the aeroacoustic emissions at the trailing edge, the difference observed here experimentally indicates that results obtained from numerical studies based on the 2D flow assumption have to be considered carefully.

Moreover, in the context of laminar boundary layer instability noise, periodic amplitude modulation is observed also for the velocity fluctuations near the trailing edge. This leads to the conclusion that multiple tones can arise not only from a phase modulation of fluctuations on the pressure side and suction side, as proposed by Desquesnes *et al.* (2007), but also from a periodic modulation of the fluctuation amplitude. The presence of a periodic amplitude modulation on the pressure side, even for the case of forced transition on the suction side, confirms that a two-sided feedback loop is not a necessary condition for the presence of multiple tones.

At present, the cause for this periodic modulation remains unknown. It can only be speculated about and remains a future challenge. In view of feedback loop hypotheses that have been proclaimed by a number of researchers (Arbey & Bataille 1983; Desquesnes *et al.* 2007; Plogmann *et al.* 2013), it might be conjectured that scattering of pressure fluctuations induced by periodically modulated convecting instabilities at the trailing edge cause acoustic waves to propagate upstream. These acoustic waves might then modulate perturbations in the receptivity region and thereby support a periodically modulating feedback loop as a frequency selection mechanism for the discrete tones in the acoustic spectrum.

Acknowledgement

This research is supported by the European Communitys Seventh Framework Programme (FP7/2007–2013) under the AFDAR project (Advanced Flow Diagnostics for Aeronautical Research). Grant agreement No. 265695.

Supplementary movie

Supplementary movie available at http://dx.doi.org/10.1017/jfm.2014.156.

REFERENCES

AIZIN, L. 1992 Sound generation by a Tollmien–Schlichting wave at the end of a plate in a flow. *J. Appl. Mech. Tech. Phys.* **3**, 50–57.

AMIET, R. 1976 Noise due to turbulent flow past a trailing edge. *J. Sound Vib.* **47** (3), 387–393.

ARBEY, H. & BATAILLE, J. 1983 Noise generated by airfoil profiles placed in a uniform laminar flow. *J. Fluid Mech.* **134**, 33–47.

ARCONDOULIS, E. J. G., DOOLAN, C. J., ZANDER, A. C. & BROOKS, L. A. 2010 A review of trailing edge noise generated by airfoils at low to moderate Reynolds number. *Acoust. Austral.* **38** (3), 387–393.

ATOBE, T., TUINSTRA, M. & TAKAGI, S. 2009 Airfoil tonal noise generation in resonant environments. *Trans. Japan. Soc. Aeronaut. Space Sci.* **52** (176), 74–80.

BOUTILIER, M. S. H. & YARUSEVYCH, S. 2012 Separated shear layer transition over an airfoil at a low Reynolds number. *Phys. Fluids* **24**, 084105.

BROOKS, T. F. & HODGSON, T. H. 1981 Trailing edge noise prediction from measured surface pressures. *J. Sound Vib.* **78** (1), 69–117.

BROOKS, T. F., POPE, D. S. & MARCOLINI, M. A. 1989 Airfoil self-noise and prediction. NASA *Tech. Rep.* 1218. Reference Publication.

CHONG, T. P. & JOSEPH, P. F. 2012 Ladder structure in tonal noise generated by laminar flow around an airfoil. *J. Acoust. Soc. Am.* **131** (6), EL461–EL467.

DESQUESNES, G., TERRACOL, M. & SAGAUT, P. 2007 Numerical investigation of the tone noise mechanism over laminar airfoils. *J. Fluid Mech.* **591**, 155–182.

FINK, M. R. 1975 Prediction of airfoil tone frequencies. *J. Aircraft* **12**, 118–120.

HARRIS, F. J. 1978 On then use of windows for harmonic analysis with the Fourier transform. *Proc. IEEE* **66** (1), 51–83.

HENNING, A., KAEPERNICK, K., EHRENFRIED, K., KOOP, L. & DILLMANN, A. 2008 Investigation of aeroacoustic noise generation by simultaneous particle image velocimetry and microphone measurements. *Exp. Fluids* **45**, 1073–1085.

HERSH, A. S. & HAYDEN, R. E. 1971 Aerodynamic sound radiation from lifting surfaces with and without leading-edge serrations. NASA *Tech. Rep.* 114370. Contr. Rep.

HOWE, M. S. 1978 A review of the theory of trailing edge noise. *J. Sound Vib.* **61** (3), 437–465.

HUTCHESON, F. V. & BROOKS, T. F. 2002 Measurement of trailing edge noise using directional array and coherent output power methods. In *Eighth AIAA/CEAS Aeroacoustics Conf. Breckenridge, Colorado*.

IKEDA, T., ATOBE, T. & TAKAGI, S. 2012 Direct simulations of trailing-edge noise generation from two-dimensional airfoils at low Reynolds numbers. *J. Sound Vib.* **331** (3), 556–574.

VAN INGEN, J. & KOTSONIS, M. 2011 A two-parameter method for e^N transition prediction. In *Sixth AIAA Theoretical Fluid Mechanics Conf. Honolulu, Hawaii, vol. AIAA 2011-3928.*

JONES, L. E. & SANDBERG, R. D. 2011 Numerical analysis of tonal airfoil self-noise and acoustic feedback-loops. *J. Sound Vib.* **330**, 6137–6152.

KINGAN, M. J. & PEARSE, J. R. 2009 Laminar boundary layer instability noise produced by an aerofoil. *J. Sound Vib.* **322**, 808–828.

LOWSON, M. V., FIDDES, S. P. & NASH, E. C. 1994 Laminar boundary layer aeroacoustic instabilities. *AIAA Paper (94-0358).*

LOWSON, M. V., MCALPINE, A. & NASH, E. C. 1998 The generation of boundary layer instability noise on aerofoils. *AIAA Paper (98-0626).*

MCALPINE, A., NASH, E. C. & LOWSON, M. V. 1999 On the generation of discrete frequency tones by the flow around an aerofoil. *J. Sound Vib.* **222** (5), 753–779.

MORRIS, S. C. 2011 Shear-layer instabilities: particle image velocimetry measurements and implications for acoustics. *Annu. Rev. Fluid Mech.* **43** (1), 529–550.

NAKANO, T., FUJISAWA, N. & LEE, S. 2006 Measurement of tonal-noise characteristics and periodic flow structure around NACA 0018 airfoil. *Exp. Fluids* **40**, 482–490.

NASH, E. C., LOWSON, M. V. & MCALPINE, A. 1999 Boundary layer instability noise on airfoils. *J. Fluid Mech.* **382**, 27–61.

PATERSON, R. W., VOGT, P., FINK, M. R. & MUNCH, C. 1973 Vortex noise of isolated airfoils. *J. Aircraft* **10** (5), 296–302.

PLOGMANN, B., HERRIG, A. & WÜRZ, W. 2013 Experimental investigations of a trailing edge noise feedback mechanism on a NACA 0012 airfoil. *Exp. Fluids* **54**, 1480.

RAFFEL, M., WILLERT, C. E., WERELEY, S. T. & KOMPENHANS, J. 2007 *Particle Image Velocimetry. A Practical Guide*. 2nd edn. Springer.

ROGER, M. & MOREAU, S. 2010 Extensions and limitations of analytical airfoil broadband noise models. *Intl J. Aeroacoust.* **9** (3), 273–305.

SANDBERG, R. D. & JONES, L. E. 2011 Direct numerical simulations of low Reynolds number flow over airfoils with trailing edge serrations. *J. Sound Vib.* **330**, 3818–3831.

SANDBERG, R. D., JONES, L. E., SANDHAM, N. D. & JOSEPH, P. F. 2009 Direct numerical simulations of tonal noise generated by laminar flow past airfoils. *J. Sound Vib.* **320**, 838–858.

SCARANO, F. 2003 Theory of non-isotropic spatial resolution in PIV. *Exp. Fluids* **35**, 268–277.

SCHRÖDER, A., HERR, M., LAUKE, T. & DIERKSHEIDE, U. 2006 A study on trailing edge noise sources using high-speed particle image velocimetry. In *New Results in Numerical and Experimental Fluid Mechanics V* (ed. H. J. Rath, C. Holze, H.-J. Heinemann, R. Henke & H. Hönlinger), pp. 373–380. Springer.

SHANNON, D. & MORRIS, S. C. 2006 Experimental investigation of a blunt trailing edge flow field with application to sound generation. *Exp. Fluids* **41** (5), 777–788.

TAKAGI, S. & KONISHI, Y. 2010 Frequency selection mechanism of airfoil trailing-edge noise. *J. Aircraft* **47** (4), 1111–1116.

TAM, C. K. W. 1974 Discrete tones of isolated airfoils. *J. Acoust. Soc. Am.* **55** (6), 1173–1177.

TAM, C. K. W. & JU, H. 2012 Aerofoil tones at moderate Reynolds number. *J. Fluid Mech.* **690**, 536–570.

TORRENCE, C. & COMPO, G. 1998 A practical guide to wavelet analysis. *Bull. Am. Meteorol. Soc.*

WELCH, P. D. 1967 The use of fast Fourier transform for the estimation of power spectra: a method based on time averaging over short, modified periodograms. *IEEE Trans. Audio Electroacoust.* **15**, 70–73.

WRIGHT, S. E. 1976 The acoustic spectrum of axial flow machines. *J. Sound Vib.* **45** (2), 165–223.